STRUCTURE AND BIOCOMPATIBILITY ANALYSIS OF SOL-GEL PREPARED NIOBIUM AND TITANIUM OXIDE WITH TEMPERATURE

BY

DIMPLE PRADHAN

A THESIS
SUBMITTED TO THE FACULTY OF

ALFRED UNIVERSITY

IN PARTIAL FULFILLMENT OF THE REQUIREMENTS
FOR THE DEGREE OF

MASTER OF SCIENCE

IN

MATERIAL SCIENCE AND ENGINEERING

ALFRED, NEW YORK

JUNE, 2012

STRUCTURE AND BIOCOMPATIBILITY ANALYSIS OF SOL-GEL PREPARED NIOBIUM AND TITANIUM OXIDE WITH TEMPERATURE

BY

DIMPLE PRADHAN

B.S. NATIONAL INSTITUTE OF TECHNOLOGY, ROURKELA (2009)

SIGNATURE OF AUTHOR_____

APPROVED BY_____

NATHAN P. MELLOTT, ADVISOR

_____

MATTHEW M. HALL, ADVISORY COMMITTEE

_____

SCOTT T. MISTURE, ADVISORY COMMITTEE

_____

CHAIR, ORAL THESIS DEFENSE

ACCEPTED BY_____

DOREEN D. EDWARDS, DEAN
KAZUO INAMORI SCHOOL OF ENGINEERING

ACKNOWLEDGMENTS

First of all, I would like to express my deepest gratitude to my thesis advisor, Dr Nathan.P.Mellott for his continuous support and guidance. With his constant motivation I have grown from strength to strength in every aspect of my work. Thank you for allowing me the freedom to work my way out and being there as and when needed to provide all possible assistance. I have learnt so much from you and will be carrying in forward with me as I go from here. You are a perfect mentor anyone can ever get.

I would also like to thank Dr Misture and Dr Wren for their help. A large part of my thesis could not be completed without your invaluable suggestion and timely guidance.

I would also like to thank Swavek Zdzieszynski and Gerald Wynick for training me to use the instruments and giving their valuable inputs for my work.

I would like to express my thanks to my friends Laura and Ian who are like family to me. I also would like to extend my thanks to my friends Fiona, Jordan and John Rich for all their support professionally and personally.

Finally, I am thankful to my Father, Mother and Amchung for their unwavering support over these years and I would like to dedicate this work to my father Mr. Raju Pradhan who has taught me invaluable lessons for life.

TABLE OF CONTENTS

LIST OF TABLES

Page

LIST OF FIGURES

Page

ABSTRACT

Niobium and titanium oxides were prepared via the sol-gel technique. The structural evolution of these oxides with calcination temperature (150-650^{o}C) was investigated using differential thermal analysis (DTA), high temperature x-ray diffraction (HTXRD), and Raman spectroscopy. The phase transformations of the niobium oxide as a function of calcination temperature were as follows; amorphous to hexagonal (~500^{o}C) and hexagonal to orthorhombic (~600^{o}C). The crystallite size increased from 23 to 74 nm. The titanium oxide remained amorphous to 325^{o}C until crystallization to the tetragonal anatase phase at ~350^{o}C, and remained so until 650^{o}C. The anatase crystallite size increased from 22 to 45 nm. The lattice parameters and cell volumes for both niobium and titanium oxides were determined using the Rietveld method from which the linear and volume thermal expansion coefficients were calculated respectively. Raman spectroscopy was used to further characterize the structure of these oxides and both band position and shape were strongly dependent on calcination temperature, with overall results consistent with HTXRD.

A series of selected oxide compositions and structures including; TiO_2-amorphous (275^{o}C), TiO_2-tetragonal (500^{o}C), Nb_2O_5-amorphous (450^{o}C), Nb_2O_5-hexagonal (525^{o}C), and Nb_2O_5-orthorhombic (650^{o}C), were then selected for bioactivity testing using simulated body fluid (SBF) analysis. Bioactivity was determined through the analysis of calcium phosphate formation at the surface of selected oxides as a function of SBF reaction time, as observed under Scanning Electron Microscopy (SEM) and Energy Dispersive X-Ray Spectroscopy (EDX). It was shown that bioactivity was a function of crystallinity, as TiO_2-tetragonal (500^{o}C), and Nb_2O_5-hexagonal (525^{o}C) were the only oxides which exhibited bioactivity.

I. INTRODUCTION

Transition metal oxides represent an important class of materials that have enormous technological importance, and hence have been extensively studied over the past several decades[1]. This has resulted in the use of transition metal oxides in a wide variety of material systems ranging from optoelectronic components in the form of electrochromic devices and capacitors to bioactive coatings on orthopedic implant materials[2]. Of particular interest in this thesis are transition metal oxides for biomaterial applications. Two important oxides for biomaterials are niobium and titanium oxide, in particular as potential candidates as biocompatible coatings.

1. Biocompatible materials

Artificial implants are typically made of stainless steel or titanium alloy and can be used for dental implants, hip joint prosthesis and coronary stents[3]. While these metal implants have the required mechanical properties, they are bioinert and cannot directly bond to bone, therefore hindering their practical use[4,5]. When metal implants are placed in the body; metal ions are released, infiltrating living tissue and causing adverse biological effects. Degradation of implants in the corrosive biological environment causes the formation of fibrous tissue between the implant and bone. This weak bonding results in the reduction of strength of the implants and in the case of load bearing implants leads to its failure[4]. These complications can often be mediated through the addition of a bioactive coating onto the metal implant. Such coatings cause tremendous improvement in the bonding of the implant with the surrounding tissues[6].

A wide range of materials have been shown to be biocompatible; of particular interest here are niobium and titanium oxide[4,7-9]. The biological properties of materials are dominated by their chemical, physical and physicochemical properties; for example, Nb_2O_5 shows extremely high corrosion resistance and thermodynamic stability[2,10]. However, this material has received little attention in the biomaterial literature[2,4,9,11].
On the other hand, titanium dioxide (TiO_2) has been studied as a biomaterial for many years, and has found success as the material of choice for antiviral coating (TiO_2-coated

ceramic plate), cancer-cell treatment (TiO_2 nanotubes)[12], bone regeneration (hydroxyapatite/TiO_2)[13], sunscreen agents in cosmetics (TiO_2-coated mica platelets)[14], and antibacterial coatings (Ag–TiO_2–chitosan complex)[15] . Furthermore, titanium based metals and alloys are also utilized in medical applications as they often form a thin oxide layer of TiO_2 which interacts with the living environment, improving the bioactivity of the implant. However, this naturally formed oxide layer is irregular and not efficient for long term applications[3]. Therefore, even in the case of titanium metal implants it is often necessary to coat the metallic implants with oxides to make them more durable[3]. The coatings should not show any inflammatory response, exhibit low toxic effects and provide good biocompatibility and corrosion resistance. In addition, the material should be bioactive, have a low elastic modulus and high hardness. Porous, nanocrystalline implant coatings are beneficial to promoting osteoblast attachment and proliferation as well as acceleration of osseointegration[6]. Also when the artificial implant is coated with a low elastic modulus substance it can eliminate stress-shielding, promoting bone remodeling and prevent implant fracture[6]. Thus, the bioactive coatings provide a stable interface between the implant and surrounding tissue which increases their durability[3].

A. Bioactivity testing using simulated body fluid (SBF)

There are a number of methods which have been developed to test the biocompatibility of oxides coatings; one of the most accepted is simulated body fluid (SBF) testing[7,8,16]. In 1991, it was proposed that for a bioactive material the essential requirement is the formation of a bone like apatite layer on the surface of an implant upon bonding to living bone. The environment of living bone can be reproduced artificially through controlled chemistry of simulated body fluid (SBF). Hence, a material is often termed “bioactive” if an apatite layer is formed upon interaction of the material to SBF[16].

Table I. Ion Concentration in SBF in Comparison with Those in Human Blood Plasma

Ion	Ion concentration (mM)	
	Blood plasma	SBF
Na^+	142.0	142.0
K^+	5.0	5.0
Mg^{2+}	1.5	1.5
Ca^{2+}	2.5	2.5
Cl^-	103.0	147.8
HCO_3^-	27.0	4.2
HPO_4^{2-}	1.0	1.0
SO_4^{2-}	0.5	0.5
pH at 37°C	7.2-7.4	7.40

SBF does not contain any cells or proteins, which means that the apatite layer is formed only through the chemical reaction of the bioactive ceramics with the surrounding fluid. Table I shows the comparison of ion concentration in SBF and human blood plasma[16]. It is therefore expected that novel bioactive materials can be designed by controlling the chemical reactivity of the materials in SBF.

In addition to the SBF composition shown above Table I, there are several SBF compositions proposed by different researchers[17,18]. However, none of these solutions correspond to the composition of human blood serum. The three main differences between SBF solutions and serum are (i) the absence of proteins, whereas they are known to play an essential role in controlling apatite nucleation (nucleation inhibitors) (ii) the addition of TRIS to buffer SBF solutions, and (iii) the absence of control of the carbonate content of SBF solutions, although carbonates act as pH buffer in serum. In

spite of this SBF testing is considered one of the important tests in vitro for bioactivity of materials.

B. Apatite formation in SBF

The mechanism of nucleation and growth of apatite formation is not fully understood. However, it is believed that when a bioactive material is immersed in SBF solution the hydroxyl groups (-OH) are easily formed at the surface due to absorption of water by the oxide. In SBF solution with pH ≈ 7.4, the surfaces of metal oxides are initially negatively charged. This negatively charged surface combines with positively charged calcium ions from the SBF. The calcium ions are then adsorbed to the oxide surface causing the surface to become positively charged. Hence, the surface then proceeds to react with negatively charged phosphate ions and forms amorphous calcium phosphate. This phase is metastable and eventually forms bone-like apatite[19,20]. However, it is worth noting that Al-OH functional groups has no affinity for calcium and phosphate and do not initiate apatite formation[21]. Other functional groups such as COOH and PO_4H_2 were also found to be effective for apatite nucleation[22].

2. Material property effects on bioactivity

A. Composition effect on bioactivity

Bioactivity has been reported to be a function of material composition. Some metallic oxides such as SiO_2, TiO_2, ZrO_2 , Nb_2O_5, HfO_2 and Ta_2O_5 prepared by sol-gel method formed apatite layer on their surface when immersed in simulated body fluid whereas those containing Al_2O_3 and V_2O_5 did not[3,19]. When zirconia reinforced with alumina (ZTA) composite was immersed in SBF, apatite growth was observed only on zirconia particles confirming that zirconia was favorable for apatite nucleation[21]. V_2O_5 is considered to be toxic and cannot be used as bioactive coatings[23].

B. Structural effect on bioactivity

In addition to composition, the structure of the coating material also plays an important role in understanding their biological responses[9]. We already know that the presence of functional groups such as OH and COOH species act as nucleation centers for apatite growth at the surface of oxides[8,20]. Acid or base treated metal oxides show

greater presence of OH groups at their surface than untreated oxides and consequently their apatite forming ability after soaking in SBF is amplified [21]. It was reported that TiO_2 soaked in NaOH at 60^{o}C for 24 hours showed greater apatite forming ability than TiO_2 without base treatment. It has been reported that a porous structure with submicron pore size and a negatively charged oxide surface are required for apatite nucleation[24]. Furthermore, it has been proposed that the presence of surface crystallinity can improve the biological response of oxides. For example, niobium oxide showed better biocompatibility when present in crystalline versus amorphous form[9]. Furthermore, it has been shown that anatase phase of TiO_2 nanoparticles exhibited greater apatite formation than rutile or amorphous phases[7]. In addition, it has been reported that a rough surface and high surface area can facilitate nucleation of apatite, while the presence of organic residue at the oxide surface which are insoluble in SBF inhibit apatite formation[25,9].

3. Niobium and titanium oxide structure

There have been great efforts to observe the detailed structural changes occurring within metal oxide systems with temperature. One technique which has proven particularly useful is high temperature x-ray diffraction (HTXRD), which has the ability to directly monitor detailed structural changes occurring with temperature[26]. The HTXRD analysis eludes problems of uneven heating time and allows measurement in their actual working environment; with phase identification and transformation temperatures often evaluated using the technique. Rietveld refinement, when performed on the data, calculates crystallite size and lattice constants which, in turn, can help in obtaining coefficient of thermal expansion[27].

In addition, Raman spectroscopy has also been shown to be useful in the investigation of metal oxides[28-32]. Raman spectroscopy is very sensitive to structure and short range bond order, and therefore, is an important tool for understanding the structural evolution and bonding environment of metal oxides[29]. The relationship between various metal oxide structures and their corresponding Raman spectra have been reported[29,32]. The structural distortion associated with crystal phase transformations result in major shifts in Raman bands[1].

Niobium pentoxide (Nb_2O_5), the most common niobium based oxide, possesses complex crystalline transformations as a function of temperature, with as at least 12 structures previously identified[33]. The most common phases are typically referred to as T (orthorhombic), TT (hexagonal), and H (monoclinic) phases, with their appearance depending upon the preparation method of the compound and the kinetics and thermodynamics associated with formation[29]. The phases obtained as a function of temperature is as follows; an initially amorphous phase, upon heating, crystallizes to the hexagonal phase (TT- N_2O_5) at or above approximately 400^oC , followed by an orthorhombic phase (T- N_2O_5) which forms at ~600 to 800^oC, then finally at higher temperatures the monoclinic structure is formed (H-Nb_2O_5)[29].

Amorphous $\Longrightarrow$ Hexagonal $\Longrightarrow$ Orthorhombic $\Longrightarrow$ Monoclinic

(*Conversion temperature varies*)

In particular, the hexagonal phase consists of an oxygen deficient unit cell forming tetragonal and pentagonal bipyramids with six or seven oxygen atom coordination[29]. The orthorhombic structure forms distorted tetragonal or pentagonal bipyramids with six or seven oxygen coordinated to a Nb atom. The monoclinic form is thermodynamically the most stable form of all[29]. The hexagonal phase is thought to be a modification of the orthorhombic T phase as it presents a lower crystallinity and is most likely stabilized by impurities such as OH^-, Cl^- or vacancies[34].

As with niobium oxide, the properties of titanium oxide significantly depend on its crystalline phases; namely anatase, rutile and brookite[35]. Anatase and rutile are tetragonal while brookite is orthorhombic[32]. The titanium ion coordinates with six oxygen ions. At high calcination temperature the anatase and brookite form undergoes transformation to form the rutile phase[32]. The crystal structures of both anatase and rutile are given in Figure 1. The phase transformation (anatase to rutile in particular) is particle size dependent (below ~14nm anatase phase is more stable)[36]. In addition to its dependence on heat treatment temperature, the phase formation is also governed by fabrication methods, impurity content, reaction atmosphere, and heat treatment

temperature[36]. For example, irradiation of TiO_2 powder by UV pulsed lasers also promotes phase transformation in titania[1].

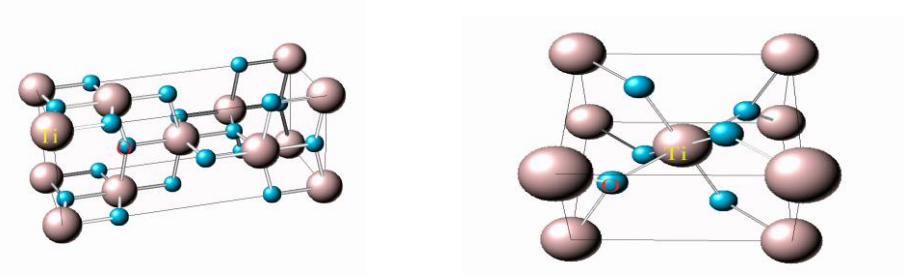

(a) (b)

Figure 1. Crystal structure of (a) anatase (b) rutile titanium oxide.

Amorphous ⟹ Anatase ⟹ Rutile

(*Conversion temperature varies*)

Tetragonal TiO_2 (anatase) is composed of TiO_6 octahedra that share two adjacent edges in the ac- and bc-planes. The anatase phase (Figure.1a) shows shortening of four shared edges and correspondingly lengthening of four unshared edges giving long elongated octahedral in the direction of c-axis[31].

4. Niobium and titanium oxide processing

Nanocrystalline metal oxides have been processed using a wide variety of preparation routes including electrochemistry[30], sputtering[2,4,11,37,38], spray pyrolysis[39,40], colloidal suspension[36] and sol gel processing [2,3,41-48]. The sol-gel method is a wet chemical route for preparation of inorganic oxides based upon the hydrolysis and condensation of molecular precursors in a solvent with or without the use of a catalyst[23]. In particular, sol-gel processing has gained impetus over others due to inherent advantages including; high purity raw materials, low processing temperature, uniform phase distribution, superior morphology control, and low cost[49].

Niobium oxide prepared via the sol-gel technique was first reported in 1985[33]. Since then, several reports for sol-gel preparation of niobium oxide powders and films can be found[42,44,46,48]. The powders obtained through sol-gel preparation are a function of precursor type and preparation method[34]. Common processing of niobium oxides

include the dissolving of precursor materials (such as $NbCl_5$ or metal alkoxide (Nb $(OC_2H_5)_5$) in a solvent, together with the addition of glacial acetic acid or HCl[42,47,48]. In particular, the choice of the molecular precursor is an important factor in the overall synthesis process. Metal salts generally contain chlorides and nitrates which may not be removed easily, often resulting in the deterioration of material properties[46]. However, metal alkoxides do not introduce such impurities, but are comparatively expensive[50]. Properties of final powders and films are strongly dependent on composition of solutions and precursors and solvents used. For example titanium oxides have been synthesized using numerous precursors including titanium alkoxides ($Ti(OBu)_4$ and $Ti(OPr)_4$), chlorides ($TiCl_3$, $TiCl_4$), and sulphates ($Ti(SO_4)_2$). As with niobium oxides, metal alkoxide precursors are typically the precursor of choice for titanium oxides as the chlorides and sulphates result in final powder or film impurities[43]. The titanium precursor is generally soluble in a solvent such as ethanol, isopropanol or butanol with or without water. It has been shown that the solvent has strong effect on crystallization behavior, porosity and microstructure of the samples[51].

5. Influence of processing technique on microstructure and properties

It is necessary to understand the influence the different preparation methods on microstructure of powders; as these, in turn substantially affect their properties. In general, the surface structure of sol-gel prepared oxides (Nb_2O_5, TiO_2 and mixed oxide of SiO_2-TiO_2) have been shown to be highly porous, with large surface roughness and minimal organic residues[3]. These properties are desirable for improving the biological response of metal oxides. Therefore, sol-gel processing is considered as one of the preferred techniques to obtain structural features needed for improving apatite forming ability of materials. It has been reported that sol-gel prepared Nb_2O_5 showed higher biocompatibility than those prepared by magnetron sputtering[2,4,9]. It has also been reported that sol-gel coating imparted higher surface OH functionalities than those produces by acid/ base treatments[52].

The time required for apatite formation is also an important parameter in describing the bioactivity of materials. A highly bioactive material is known to form Ca

and P layer in a shorter time. Sol-gel synthesized TiO_2 (anatase) showed good apatite formation after 1 day while TiO_2 prepared by sputtering films 5 days.

6. Niobium and titanium oxide bioactivity

The biocompatibility of metal oxides depends on bulk chemistry, crystal phase, particle size and degree of crystallinity[7]. It was reported that apatite formation on TiO_2 nanoparticles was greater for anatase (crystallite size ~11.25 nm) than rutile (crystallite size ~39.46 nm) and the amorphous phase. Niobium oxide was reported to show greater bioactivity in crystalline than amorphous form[4,9,11]. It is well known that calcination improves crystallinity and induces phases formation in oxides[53]. Heat treatment can improve the bioactivity of metal oxides. However, very high temperature can densify the structure and reduce OH species at the surface, lowering its bioactivity[54]. Another method for improving bioactivity was by forming composites with hydroxyapatite[10]. Titania-hydroxyapatite (TiO_2-HAp) composites showed greater apatite forming ability than pure titania[8]. The apatite formation was faster on TiO_2-HAp composites containing anatase phase than rutile[8]. Niobium–apatite composite show improved biocompatibility and biomechanical properties than pure Nb_2O_5 and HAp respectively[10].

In this thesis, amorphous niobium and titanium oxide powders were successfully prepared using alkoxide-based sol-gel preparation methods. The influence of heat treatment on the structure and phases of the oxides were then investigated using various in-situ and ex-situ materials characterization techniques. Five different oxides, all with different crystal structures, were then tested for their bioactivity through SBF testing followed by SEM and EDAX analysis. Through this study, we attempt to correlate oxide composition and structure to bioactivity of titanium and niobium oxides.

II. EXPERIMENTAL PROCEDURE

1. Solution preparation

The metal precursors used for sol preparation included titanium (IV) isopropoxide (Ti $(OC_3H_7)_4$) 99.99% and niobium (V) ethoxide (Nb $(OC_2H_5)_5$) 99.95%, (Sigma- Aldrich). The solvent and catalyst used were ethyl alcohol denatured (SDA proprietary solvent) and glacial acetic acid (certified by ACS plus) respectively, (Fisher scientific)[43]. The volume of individual chemicals used for sol preparation is shown in Table II.

Niobium oxide and titanium oxide sols were prepared individually. The volume of ethanol and acetic acid added in both sols were kept constant. The complete processing steps have been shown in Figure 2. First, ethanol was taken in a beaker and glacial acetic acid was added while stirring. After 15 minutes the metal precursor was added to the mixture drop wise. The solution was covered with perforated parafilm and stirred for 2 hours to obtain a homogeneous transparent solution.

Table II. The Batch Calculations for Preparation of Solutions

Chemicals	Niobium ethoxide	Ethanol	Acetic acid
Moles	0.01	1.00	0.10
Volume(ml)	2.50	58.39	5.72

Chemicals	Titanium isopropoxide	Ethanol	Acetic acid
Moles	0.01	1.00	0.10
Volume(ml)	2.96	58.39	5.72

2. Powder preparation

The stable, transparent solution was then heated at 60^{o}C with simultaneous stirring until all the liquid was evaporated and powders were obtained (36-48 hrs). This was performed for both niobium and titanium solutions.

The powders obtained were dried at 150^{o}C for 24 hrs in a Thermo Scientific Lindberg Blue M oven (model no. 6965). This was followed by a specific heating schedule given below.

The powders obtained after drying were crushed using an agate mortar and pestle to minimize agglomeration. The samples were then heated in a Thermo Scientific Thermolyne furnace (model no. F48025-6080) at temperatures from 200 to 650^{o}C with a heating rate of 20^{o}C per minute and dwell period of 90 minutes after every 25^{o}C increase in temperature. Approximately 0.3-0.5g of sample was taken out at the end of each dwell time. All samples were then crushed and stored in separate containers for further analysis.

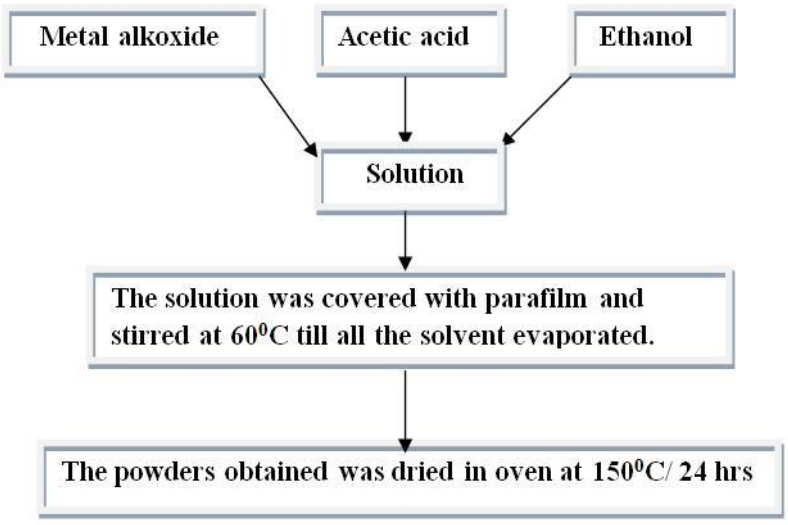

Figure 2. Schematic diagram for sample preparation.

3. Material characterization

A. Differential thermal analysis/ thermogravimetric analysis (DTA-TGA)

DTA-TGA analysis was performed using a SDT 2960 Simultaneous DSC-TGA operated in DTA-TGA mode. Approximately 14-20 mg of powders with equal amount of reference material (α-Al_2O_3) were placed in platinum crucibles. The measurements were obtained from room temperature to 850 ^oC in constant flow of air at a heating rate of 20^oC/minute.

B. High temperature x-ray diffraction

High temperature X-ray diffraction (Cu-Ka radiation) was performed using a Bruker D8 advance diffractometer equipped with a Vantec P.S detector with Gobel mirror, 1.0 mm divergence slit and Anton Paar high temperature furnace attachment. Measurements were made @ 40KV x 10mA over the scanning the range from 10 to 140° 2θ at a step size of 0.03° and scan rate of 10^oC 2θ/min. The high-temperature experiments were carried out using a heating rate of 20°C/min, with dwell period of 90 minutes after every 25°C. The measurement was taken at the end of each dwell period. Phase and space group analysis was determined using Jade 9 software (Materials Data Inc., USA).

C. Rietveld method performed on the crystalline data

The crystal structures, unit cell dimensions and site occupancy were determined from Jade 9 software (Materials Data Inc., USA) and FIND it software. Structure files or CIF files were used for refinement of titanium-based powders. However, since CIF files for hexagonal phased niobium oxide were not found, Pawley method was applied for niobium-based powders. Pawley method used peak positions instead of structure to refine the data. Initially, the scale factor, background, profile, peak shape function, zero shift, sample displacement, and lattice parameters were refined.

Reitveld refinements using TOPAS software (Bruker AXS, Germany) was performed to obtain lattice parameters, crystallite size, and strain. The background was modeled using Chebyshev's polynomials of the first kind. Refinement results were critiqued according to reasonableness of the structure and visual inspection of the

calculated and observed patterns. The weighted residual, Rwp, was also used in evaluating results.

D. Raman spectroscopy

Raman analysis was performed on a Witec Confocal Raman Microscope CRM200 equipped with Si detectors, green laser with an excitation wavelength of 532nm and power of 70mW, and a dispersion grating selected of 600l/mm. The instrument was calibrated using standard silicon, including a test run on a focus spectrum. This was performed to optimize the intensity of the beam. The characteristic Si line at 520 cm^{-1} was maximized through optimization of SMA connector. Raman spectroscopy was obtained for all heat treated samples.

E. Specific surface area and porosity analyzer

The specific surface area (SSA) of the synthesized powders was measured according to BET method with a micromeritics Tristar 3000 using N_2 as the adsorptive gas. Prior to analysis powders were degassed in a micromeritics flowprep 060 sample degas system at 150°C for 24 hours. The instrument was standardized before and after analysis using silica-alumina rods standards (SSA) of 201 ±5 m^2/g. Approximately 0.2-0.3g of powder was used for analysis.

F. SEM/EDX

Scanning electron microscopy was performed using FEI Co. Quanta 200F equipped with a field emission gun. Analyses were performed at an accelerating voltage of 12.5 kV and beam current of 26nA. In addition, semi-quantitative analysis was performed using energy-dispersive X-ray spectroscopy (EDX).

4. Bioactivity analysis

A. Simulated body fluid testing

Strategically chosen samples were tested for bioactivity via simulated body fluid (SBF) testing. The samples chosen for analysis are listed in Table III. Samples were first mechanically ground and sieved to obtain uniform sized particles below 30μm. About 1.6g of selected powders were pressed into pellets of dimensions (8.06mm x 1.3mm). The pressure applied was 1000psi with holding time of 30 seconds.

Table III. The Five Samples Tested for Biocompatibility

Chemical	**TiO_2 275°C**	**TiO_2 500°C**	**Nb_2O_5 450°C**	**Nb_2O_5 525°C**	**Nb_2O_5 650°C**
Crystal structure	amorphous	tetragonal	Amorphous	hexagonal	orthorhombic

Simulated body fluid (SBF) was produced in accordance with the procedure outlined by Kokubo et al.[16]. Reagent grade NaCl, $NaHCO_3$, KCl, $KH_2PO_4.3H_2O$, $MgCl_2.6H_2O$, $CaCl_2$, and Na_2SO_4 were dissolved in 700ml of deionized water using a magnetic stirrer. The reagent, concentration and order of dissolution are outlined in Table IV. The ion concentration in SBF closely resembles the concentration of human blood plasma, as discussed in the introduction section of this thesis. The solution was maintained at 36.5±0.5°C. The pH of the solution was adjusted to 7.4 by adding Tris (hydroxymethyl) aminomethane and 1 M-HCl. The volume of the solution was adjusted to 1 L by addition of deionized water[16]. Once prepared, the SBF solution was stored in conical flask with a stopper and kept at 5-10°C in a refrigerator. All solutions were used within 2 weeks of preparation.

Table IV. Order, Amount and Reagents for Preparation of 1000ml of SBF

Order	Reagent	Amount
1	NaCl	8.035g
2	$NaHCO_3$	0.355g
3	KCl	0.225g
4	$KH_2PO_4.3H_2O$	0.231g
5	$MgCl_{2.}6H_2O$	0.311g
6	1.0M HCl	39ml
7	$CaCl_2$	0.292g
8	Na_2SO_4	0.072g
9	Tris buffer	6.118g
10	1.0M HCl	0-5ml

1. Soaking in SBF:

The pellets were soaked in SBF for 1, 7, and 30 days. The dimensions of the pellet (diameter and height) were measured to calculate the surface area of the pellets using equation (1).

$$\text{Surface area of pellets } (S_a) = 2\pi r^2 + 2\pi rh \quad (1)$$

where 'r' is the radius and 'h' is the height of the pellet.

The volume of SBF in which the pellet is soaked depends on the surface area of the pellet. This was calculated using equation (2).

$$\text{Volume of SBF } (V_{SBF}) = S_a / 10 \quad (2)$$

After soaking, pellets were removed from the solution, gently rinsed with deionized water and stored in incubator at 37^oC for 24 hours. The pellets were then analyzed using SEM/EDX.

III. RESULTS AND DISCUSSION

1. Processing

Niobium and titanium-based sols obtained in this work were both transparent and stable. Following solution evaporation the as-prepared titanium-based powders appeared pale yellow, while niobium-based powders appeared off-white. Upon grinding and heating to 150^{o}C for 24 hours, fine, white powders resulted. These powders, from this point forward will be referred to as cured powders. Both as-prepared and cured powders are shown in Figure 3.

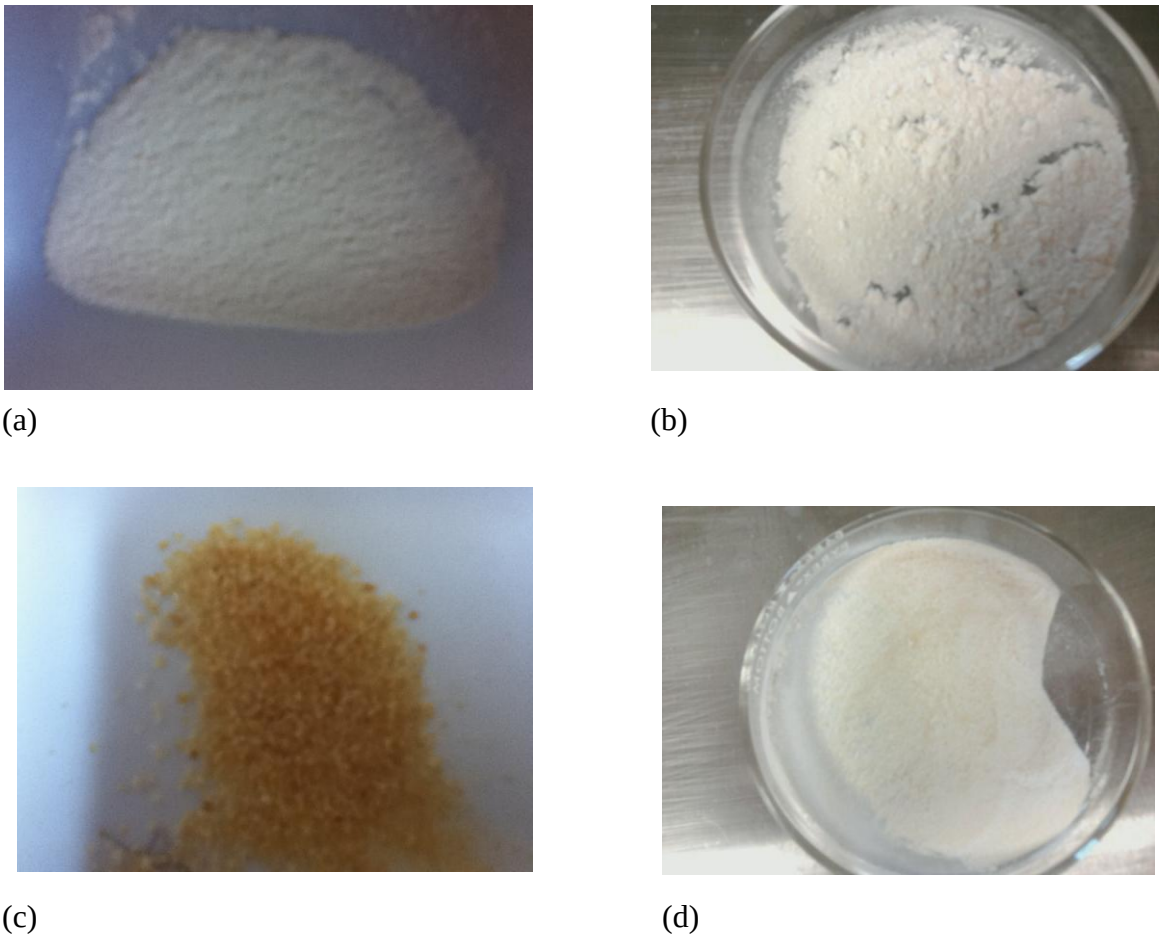

(a) (b)

(c) (d)

Figure 3. Digital images of (a) as-prepared niobium-based powders, (b) cured niobium- based powders, (c) as-prepared titanium-based powder, and (d) cured titanium-based powders.

It is worth noting here that this preparation method proved to be reproducible and produced powders free of contamination.

2. Material Characterization

A. DTA/TGA

DTA/TGA analysis was used to determine stability ranges and to guide high temperature heat treatment parameters. DTA/TGA analyses of cured niobium- and titanium-based powders are shown in Figure 4 (a) and 4 (b) respectively.

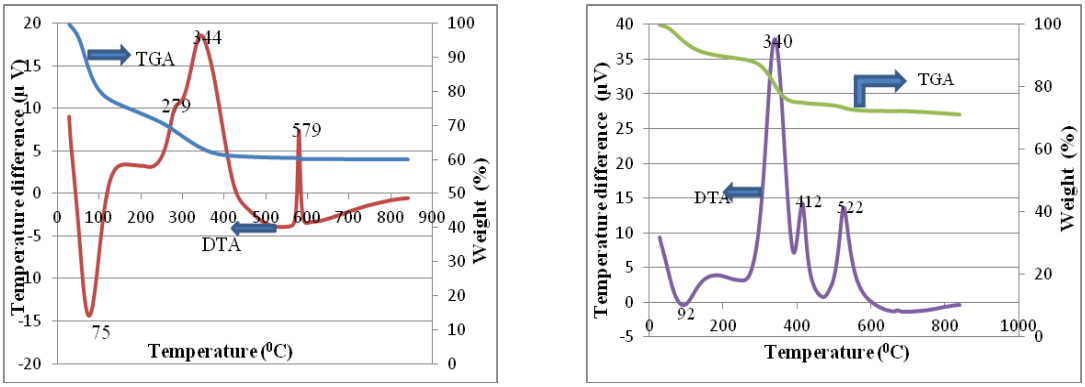

(a) (b)

Figure 4. DTA/TGA plots for cured (a) niobium-based and (b) titanium-based powders.

For niobium-based powders, an endotherm is observed at 75^{o}C and exotherms are observed at approximately 279, 344 and 579^{o}C (Figure 4 a). Figure 4 (a) also shows gradual weight loss between 27 and 400 ^{o}C, with minimal weight loss observed between ~400 and 850^{o}C. The total weight loss for niobium-based powders when heated between 27 and 850^{o}C was ~40%.

For niobium-based powders, the first endotherm at 75^{o}C is attributed to elimination of adsorbed water and was associated with weight loss of ~25%. This is in agreement with the reports stating that removal of physically adsorbed water associated with large weight loss occurred between 70 - 230^{o}C[46,47].

The two exotherms observed at approximately 279 and 344^{o}C were due to removal of organic species and were associated with weight loss of ~10%. The exact

identities of organic species were unknown as mass spectroscopy was not performed along with DTA/TGA. However, DTA/TGA performed with mass spectroscopy for sol-gel prepared powders using $NbCl_5$ and butanol as precursor and solvent respectively with addition of acetic acid reported the removal of C_3H_7, C_4H_8, H_2O, HCl and CH_2OH at ~220^oC and exothermic peaks between 400 - 530^oC were due to removal of C_3H_7, C_4H_8 at 410^oC along with CO_2 and HCl at 450 and 530^oC respectively[47].

The sharp peak at 579^oC corresponded to transformation from amorphous to hexagonal phase (TT-Nb_2O_5). This peak was associated with minimal weight loss. This transformation temperature has been previously reported to be around 400 - 500^oC and is a strong function of molecular precursor and heating rate used[42,47]. The exact effect of heating rate could not be explained as the variation in transformation depended on synthesis history as well[41].

Niobium oxide undergoes transformation from hexagonal phase (TT-Nb_2O_5) to orthorhombic phase (T-Nb_2O_5) at higher temperature ~600^oC. However, this transformation was not observed by DTA/TGA. The reason could be that TT phase is simply a less crystalline form of T phase, therefore no significant exotherm is observed[46].

For titanium-based powders an endotherm is observed at 92^oC while exotherms are observed at approximately 340, 412 and 522^oC (Figure 4 b). Figure 4 (b) also shows gradual weight loss between 27 and 400^oC, with minimal weight loss observed between 400 and 850^oC The total weight loss for titanium -based powders when heated between 27 and 850^oC was ~30%.

For titanium-based powders, an endotherm observed at 92^oC due to removal of water was associated with weight loss of ~10%. This is consistent with previous studies which shows desorption of physically adsorbed water occurs between 70 - 200^oC with associated weight loss of 8-10%[53,55,56].

Two exothermic peaks at approximately 340^oC and 412^oC were associated with weight loss of ~15%. The former peak was broad and could be due to removal of organic species. Since mass spectroscopy was not preformed along with the DTA/TGA analysis the organic compounds removed could not be identified. However it has been reported that organic species are usually compounds of alcohol and adsorbed acetic

acid[30,55]. A single broad peak instead of two exotherms has also been reported suggesting slow crystallization with simultaneous removal of organic species[55,56].

The sharp peak at 412^{o}C is most likely associated with the phase transformation from amorphous to anatase-TiO_2 as past authors have reported the crystallization temperature to be between 300- 400^{o}C[43,56].

The sharp exothermic peak at 522^{o}C , associated with weight loss of ~5% is most likely due to the phase transformation from anatase to rutile as many authors have confirmed this transformation to be around 600^{o}C by XRD analysis[43]. However, not many DTA/TGA analyses have reported this transformation and the peaks obtained between 460 – 500^{o}C have been associated with removal of HCl and CO_2 residues[56].

B. High temp x-ray diffraction

High temperature x-ray diffraction (HTXRD) was utilized to determine phase formation and crystallographic transformation processes of powders as a function of heat-treatment temperature.

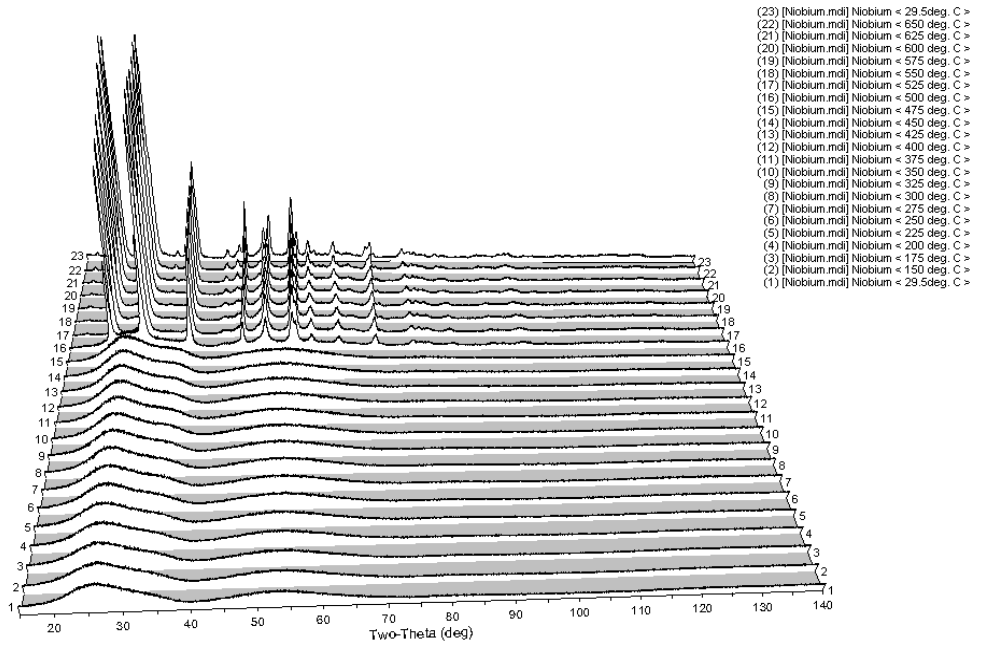

Figure 5. High temperature XRD patterns for niobium oxide from 29.5 to 650^{o}C.

The XRD patterns in Figure 5 shows the phase evolution of as-prepared niobium-based powders heated in-situ from room temperature to 650^{o}C. The powders remained x-ray amorphous up to 475^{o}C. The phase transformation from amorphous to a hexagonal phase occurred between 475 and 500^{o}C. The crystal structure then transformed to an orthorhombic phase between 575 and 600^{o}C, remaining stable until 650^{o}C.

Table V. Analysis of XRD Patterns for Niobium-Based Powders

Temperature (^{0}C)	PDF#	Chemical formula	phase	a((Å)	b((Å)	c((Å)	Space group
Rt to 475^{0}C	--------	-------	Amorphous	-------	--------	-------	---------
500^{0}C	00-028-0317	Nb_2O_5	Hexagonal	3.6070	3.6070	3.9250	PE
525^{0}C	00-028-0317	Nb_2O_5	Hexagonal	3.6070	3.6070	3.9250	PE
550^{0}C	00-028-0317	Nb_2O_5	Hexagonal	3.6070	3.6070	3.9250	PE
575^{0}C	00-028-0317	Nb_2O_5	Hexagonal	3.6070	3.6070	3.9250	PE
600^{0}C	00-030-0873	Nb_2O_5	Orthorhombic	6.1750	29.1750	3.9300	Pbam (55)
625^{0}C	00-030-0873	Nb_2O_5	Orthorhombic	6.1750	29.1750	3.9300	Pbam (55)
650^{0}C	00-030-0873	Nb_2O_5	Orthorhombic	6.1750	29.1750	3.9300	Pbam (55)

The lattice constants, space groups and phases of powders obtained after analysis of high temperature x-ray diffraction patterns for niobium-based powders are given in Table V. Niobium powders heated from 500 to 575^{o}C matched JCP file numbers 00-028-037; which corresponds to a hexagonal phase. Upon further heating, 600 to 650^{o}C, the powders transformed to an orthorhombic phase corresponding to JCP # 00-030-0873.

The HTXRD data showed the phase evolution of niobium oxide powders as a function of calcination temperature. The amorphous phase was evident from the broad hump observed from 29.5–475^{o}C. This is because as-prepared powders synthesized via the sol-gel technique are usually amorphous in nature[57]. A mixture of amorphous and crystalline phases was observed after heat treatment at 500^{o}C which was evident from

the sharp peaks and an uneven hump within the background of the pattern. Above 500°C the powders were fully crystallized to a pesudohexagonal phase (TT-Nb_2O_5). This tranformation temperature is in agreement to the temperature reported in the literature[45,58]. The crystallization temperature was dependent on the duration of heat treatment[47]. The transformation from hexagonal phase (TT-Nb_2O_5) to orthorhombic phase (T- Nb_2O_5) above ~600°C is in agreement with the value reported by different authors[46,59]. The crystallite size for T- Nb_2O_5 increased from 54 nm (600°C) to 74 nm (650°C).

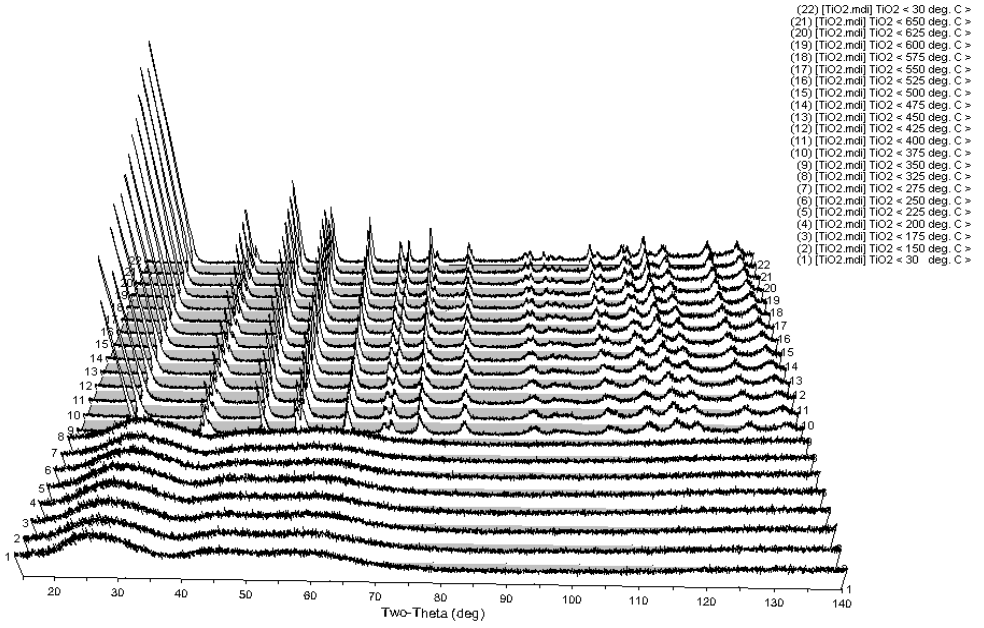

Figure 6. High temperature XRD patterns for titanium oxide 29.5 to 650°C.

The XRD patterns in Figure 6 shows the phase evolution of as-prepared titanium-based powders heated in-situ from 29.5 to 650°C. The powders remained x-ray amorphous up to 325°C. The phase transformation from amorphous to a tetragonal phase occurred between 325 and 350°C. The powders remained tetragonal until 650°C.

Table VI. Analysis of XRD Patterns for Titanium-Based Powders

Temperature (^{0}C)	PDF#	Chemical formula	Phase	a((Å)	b((Å)	c((Å)	Space group
Amorphous 350^{0}C to 650^{0}C	--------- 04-006-9240	--------- TiO_2	---------- tetragonal	--------- 3.7838	------- 3.7838	-------- 9.4950	---------- I41/amd (141)

The lattice constants, space groups and phases of powders obtained after analysis of in- situ high temperature X-ray diffraction patterns for titanium-based powders are given in Table VI. The titanium oxide powers were identified by JCPDS File No. 04-006-9240 which corresponds to a tetragonal crystal structure (anatase).

The HTXRD data showed the phase evolution of titanium oxide powders as a function of calcination termperature. The patterns revealed an amorphous phase from 29.5 to 325^{o}C. The crystallization from amorphous to anatase phase occurred above 325^{o}C; this is in agreement with the reports which suggested the transformation temperature range is 300-400^{o}C[57,60,61]. The synthesized TiO_2 powders consisted of anatase phase up to a calcination temperature of around 650^{o}C. Several authors have reported the transformation from anatase to rutile at temperature > 600^{o}C.

C. Rietveld method

Rietveld analysis of the diffraction patterns collected via HTXRD allows lattice parameters, crystallite size and cell volume to be determined. Figure 7 shows the experimental, refined, and difference patterns of niobium-based powders when heat treated from 500 to 650^{o}C. Rietveld analysis was performed via the hkl phase Pawley method, using space groups PE for the hexagonal phase and Pbam (55) for the orthorhombic phase.

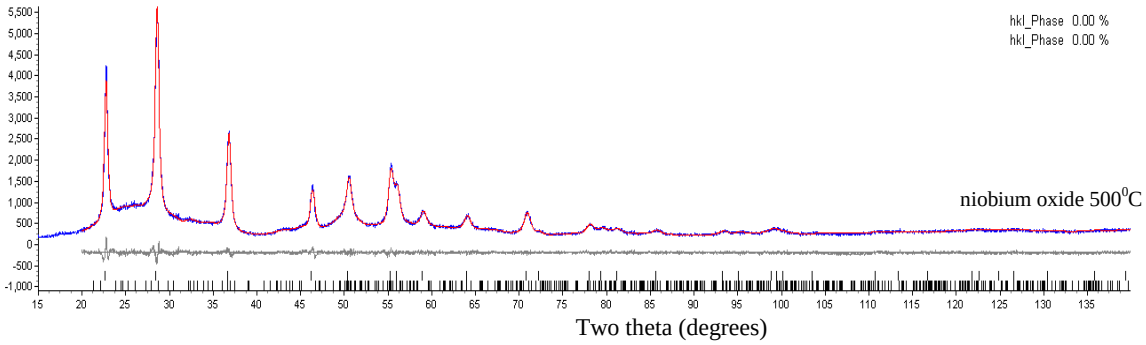

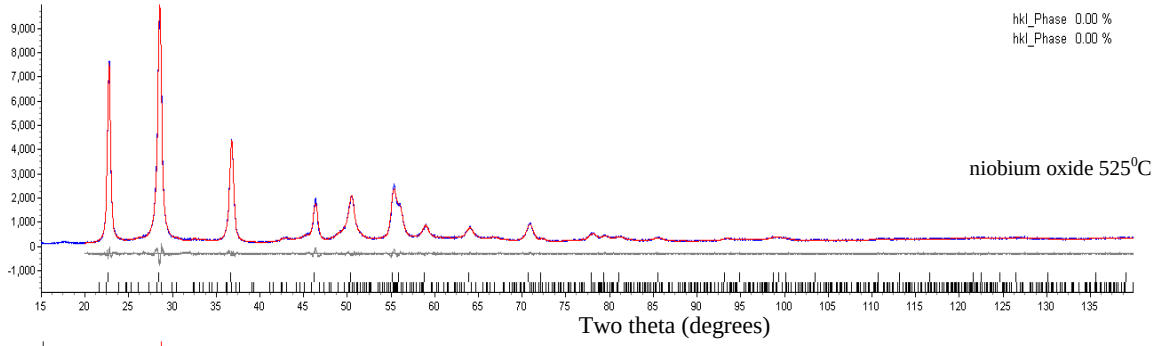
hkl_Phase 0.00 %
hkl_Phase 0.00 %
niobium oxide 525^{0}C
Two theta (degrees)

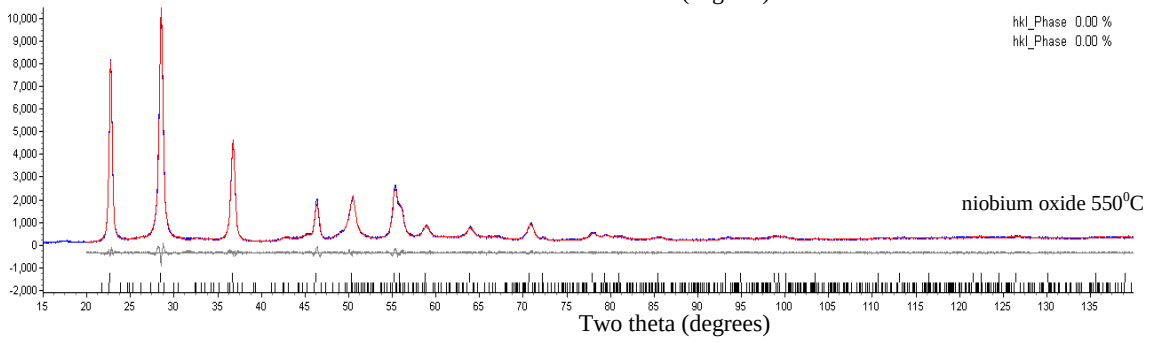
hkl_Phase 0.00 %
hkl_Phase 0.00 %
niobium oxide 550^{0}C
Two theta (degrees)

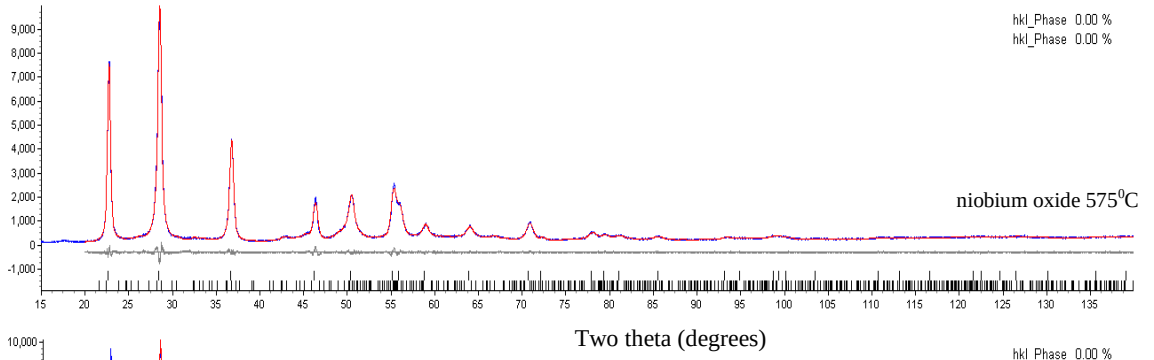
hkl_Phase 0.00 %
hkl_Phase 0.00 %
niobium oxide 575^{0}C
Two theta (degrees)

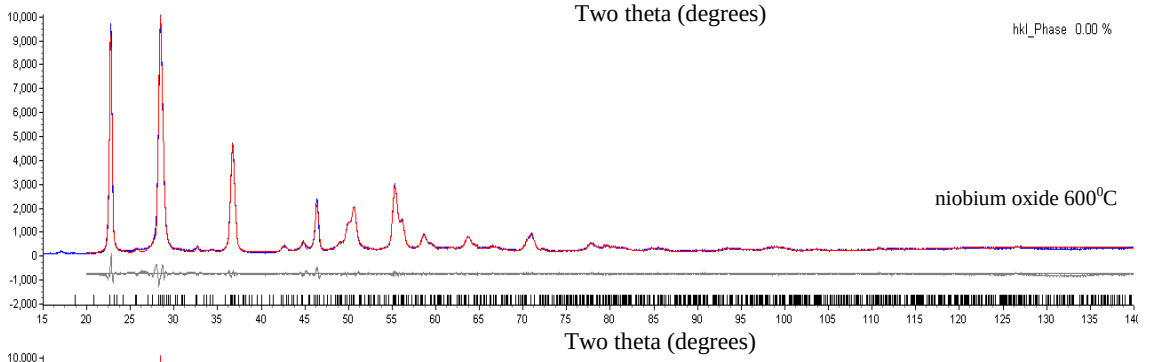
hkl_Phase 0.00 %
niobium oxide 600^{0}C
Two theta (degrees)

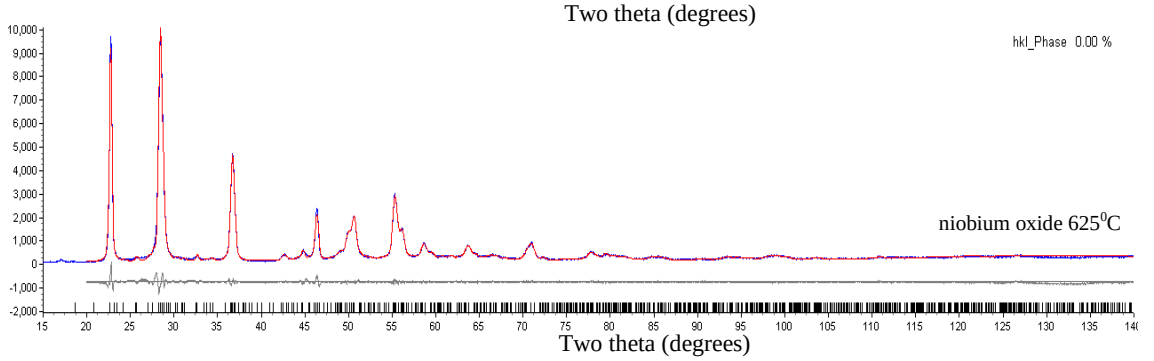
hkl_Phase 0.00 %
niobium oxide 625^{0}C
Two theta (degrees)

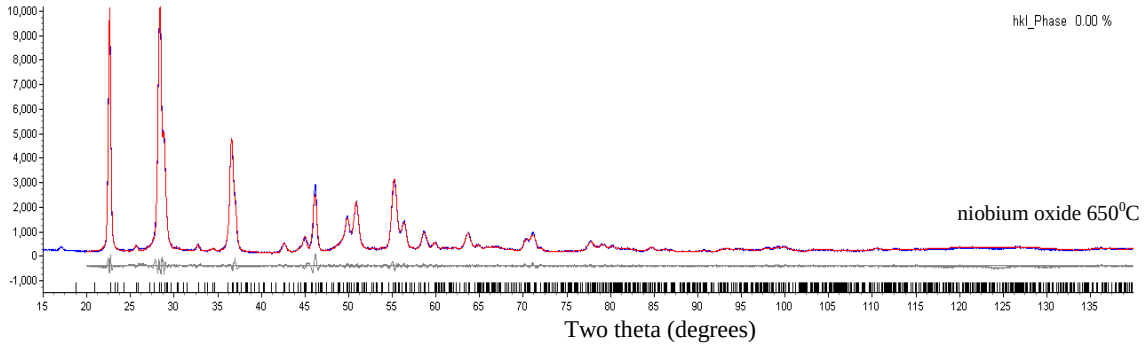

Figure 7. Refinement of niobium oxide powders as a function of heat-treatment temperature.

Table VII. Rietveld Derived Lattice Parameters, Cell Volumes and Goodness of Fits

Temperature (^{0}C)	a (Å)	b (Å)	C(Å)	Cell volume (Å^3)	R_{wp}
500^{0}C	3.6203(3)	3.6203(3)	3.9258(4)	44.56(1)	5.8
525^{0}C	3.6233(3)	3.6233(3)	3.9251(3)	44.63(1)	8.7
550^{0}C	3.6247(3)	3.6247(3)	3.9242(3)	44.65(1)	8.3
575^{0}C	3.6252(3)	3.6252(3)	3.9232(3)	44.67(1)	7.5
600^{0}C	6.242(5)	29.40(3)	3.924(3)	717.92(1)	7.2
625^{0}C	6.233(4)	29.39(2)	3.923(2)	719.59(1)	6.5
650^{0}C	6.221(4)	29.32(2)	3.917(2)	717.54(1)	7.0

The Rietveld derived lattice parameters, cell volumes, and refined goodness of fits (defined as Rwp) are shown in Table VII. The lattice parameters and cell volumes are highly dependent on crystal structure. The errors estimated for each measurement are shown in the bracket ().

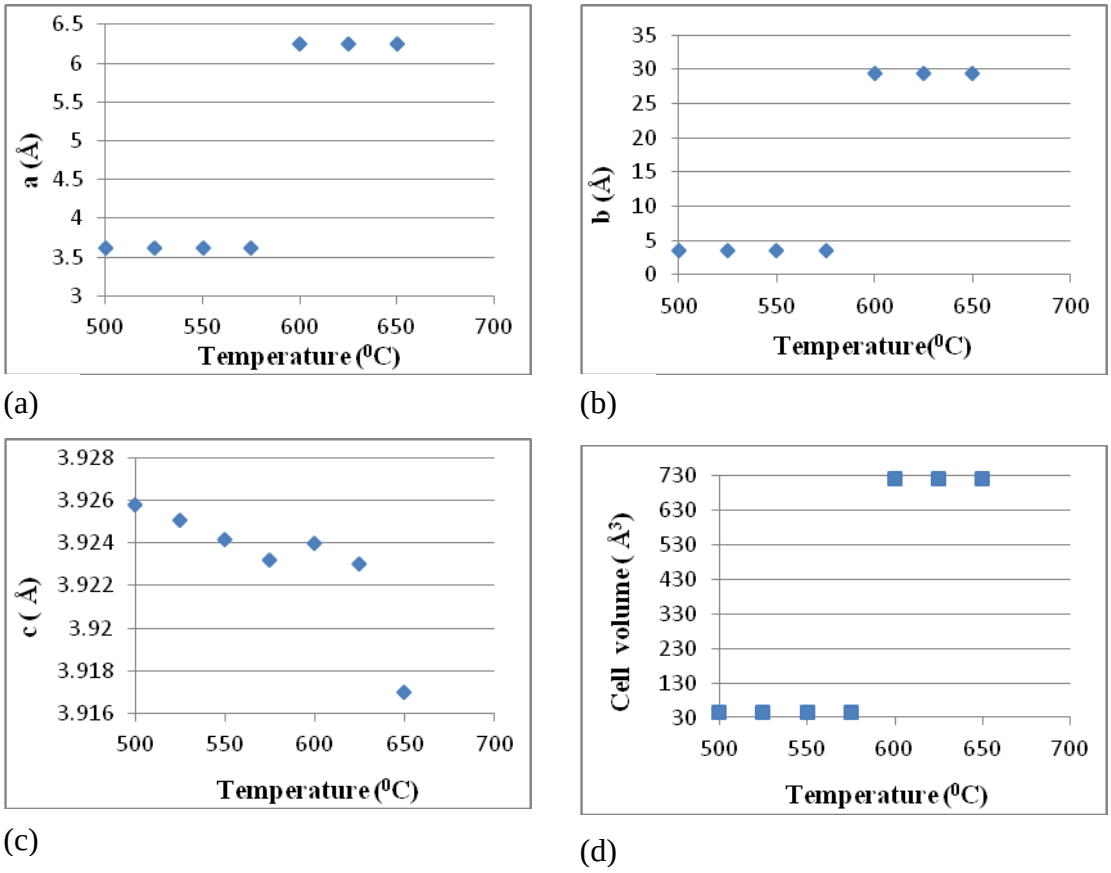

Figure 8. (a)-(c) shows change in lattice parameters and (d) unit cell volumes for niobium oxides as a function of temperature.

The graphs in Figure 8 shows change in lattice parameters and cell volume as a function of temperature. An increase in lattice parameters a and b as well as cell volume is observed with increasing heat treatment from 500 to 575^{o}C. At 600^{o}C there is an abrupt increase in lattice parameters a, b and cell volume. The lattice parameter, c on the other hand, shows continuous decrease with increase in temperature from 500-575^{o}C then it increases slightly at 600^{o}C and then decreases again up to 650^{o}C.

The graphs in Figure 8 are used to determine the linear and volume expansion coefficients as a function of temperature. This can be calculated from above graphs by using the following equations:

$$\alpha_a(T) = \frac{da}{adt} \quad (3)$$

$$\alpha_b(T) = \frac{db}{bdt} \quad (4)$$

$$\alpha_c(T) = \frac{dc}{cdt} \quad (5)$$

$$\alpha_v(T) = \frac{dv}{vdt} \qquad (6)$$

The $\frac{da}{dt}$ term was calculated by finding the slope between two different data points;

by substracting each temperature and corresponding lattice parameter from initial temperature, $t_1 = 500^0$C and lattice parameter, $a_1 = 3.6023$Å

$$\frac{da}{dt} = \frac{a_2 - a_1}{t_2 - t_1} = \frac{a_2 - 3.6023\ ^0\text{A}}{t_2 - 500\ ^0\text{C}}$$

This was performed for all lattice parameters (a, b and c) and cell volume to calculate linear thermal expansion and volume expansion coefficents.

Table VIII. Thermal Expansion Coefficients of Niobium Based Powders as a Function of Temperature

Temperature (^{0}C)	α_a ($^0C^{-1}$)	α_b ($^0C^{-1}$)	α_c ($^0C^{-1}$)	α_v ($^0C^{-1}$)
500^{0}C	———	———	———	———
525^{0}C	3.32×10^{-5}	3.32×10^{-5}	-7.13×10^{-6}	6.28×10^{-5}
550^{0}C	2.43×10^{-5}	2.43×10^{-5}	-8.15×10^{-6}	8.07×10^{-5}
575^{0}C	1.80×10^{-5}	1.80×10^{-5}	-8.83×10^{-6}	9.85
600^{0}C	0.07	0.07	-4.58×10^{-6}	0.60
625^{0}C	0.06	0.06	-5.71×10^{-6}	0.04
650^{0}C	0.05	0.05	-1.49×10^{-5}	0.04

From Table VIII it is evident that linear thermal expansion coefficients for a and b is very small and decreases for temperature range of 500^{o}C to 575^{o}C. At ~600 ^{o}C the thermal expansion coefficient increases abruptly and then it decreases up to 650^{o}C. The thermal expansion for c shows negative values which drops for temperature up to 575^{o}C and then increases slightly at ~600^{o}C followed by decrease up to 650^{o}C. The volume expansion coefficient shows initial increase up to 575 ^{o}C followed by decrease up to 625^{o}C and remains constant until 650^{o}C.

Table IX. Crystallite Sizes as a Function of Temperature

Sample	**Crystallite size (nm)**
nb500	23(4)
nb525	31(4)
nb550	37(6)
nb575	43(3)
nb600	54(2)
nb625	63(2)
nb650	74(3)

Refined crystallite size of niobium powders as a function of heat treatment are shown in Table IX. An increase in crystallite size from 23 +/- 1 nm to 74 +/- 3 nm is observed when niobium oxide powders are heated from 500 to 650^{o}C, respectively.

Rietveld method was performed on all titanium oxide XRD patterns using CIF file TiO_2 202242 instead of hkl phase Pawley method. Rietveld analysis of the diffraction pattern collected via HT-XRD for titanium based powders in Figure 9 shows the experimental, refined, and difference patterns of titanium-based powders when heat treated from 350 to 650^{o}C. The CIF file contained space group, phase, lattice parameter and atomic positions of titanium oxide (Table X).

Table X. Data Contained in the CIF File TIO_2 202242

Phase					Anatase	
Space group					I41/amd (141)	
Lattice parameters:						
a (A^0)					3.793	
c (A^0)					9.510	
Site	Np	x	y	z	Atom	Occ
Beq						
Ti1	4	0.00000	0.25000	0.37500	Ti+4	1
1						
O1	8	0.00000	0.25000	0.16670	O-2	1

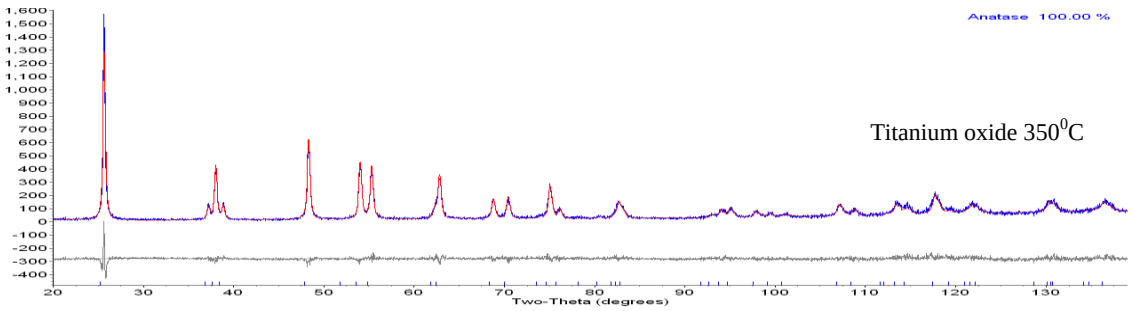

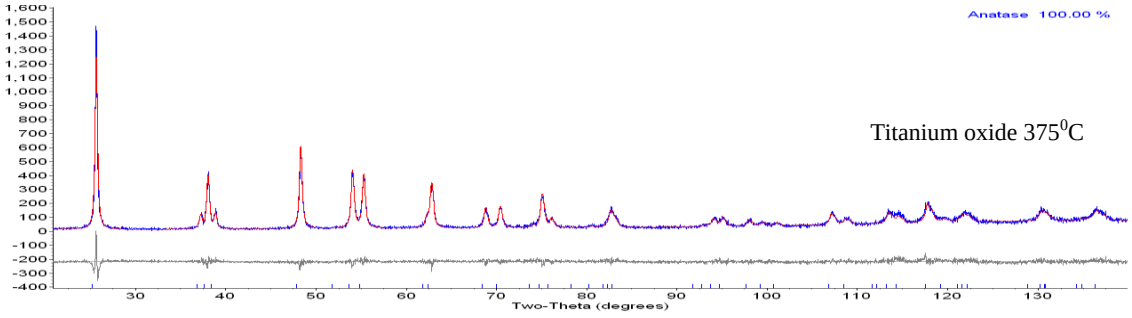
Anatase 100.00 %
Titanium oxide 375^{0}C
Two-Theta (degrees)

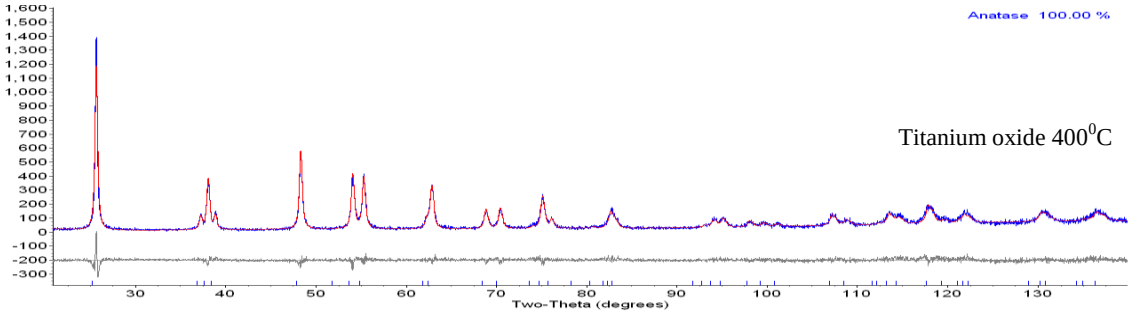
Anatase 100.00 %
Titanium oxide 400^{0}C
Two-Theta (degrees)

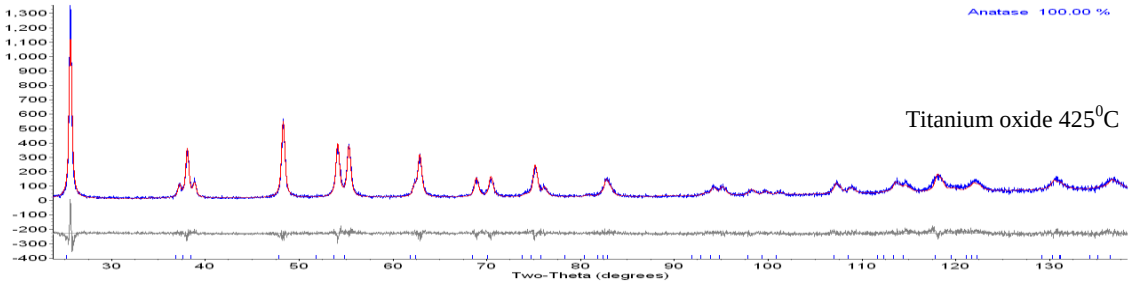
Anatase 100.00 %
Titanium oxide 425^{0}C
Two-Theta (degrees)

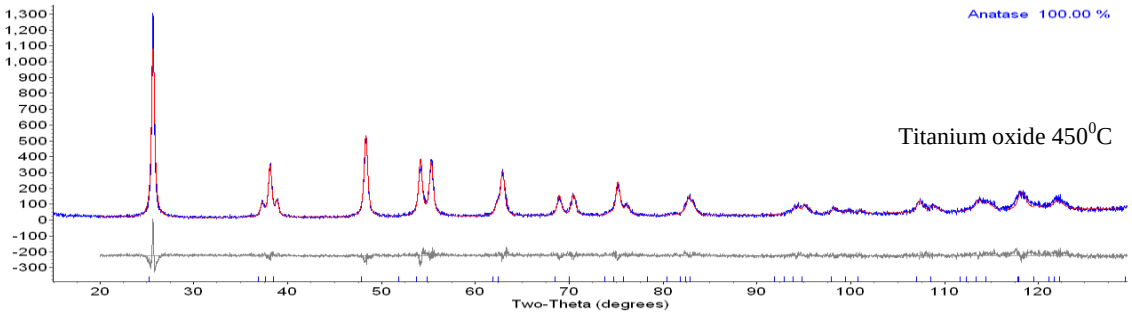
Anatase 100.00 %
Titanium oxide 450^{0}C
Two-Theta (degrees)

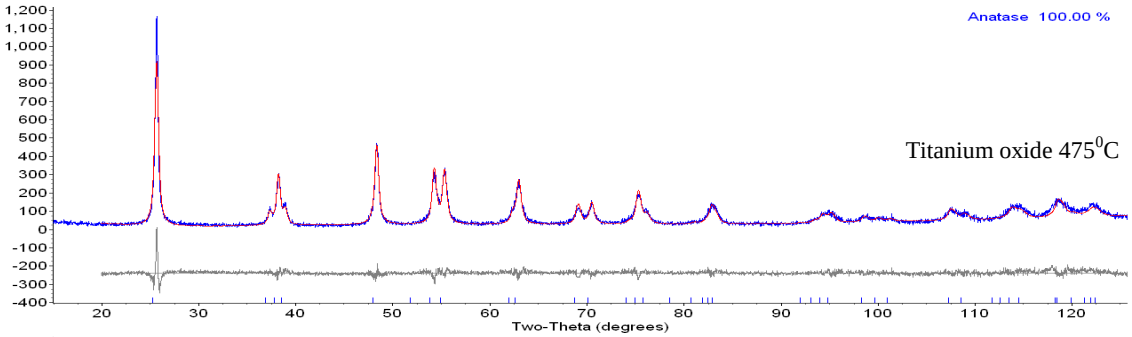
Anatase 100.00 %
Titanium oxide 475^{0}C
Two-Theta (degrees)

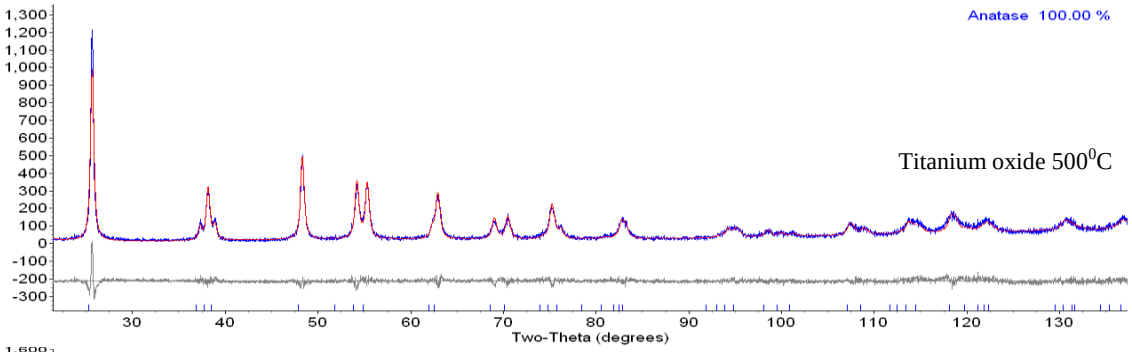
Anatase 100.00 %
Titanium oxide 500^{0}C
Two-Theta (degrees)

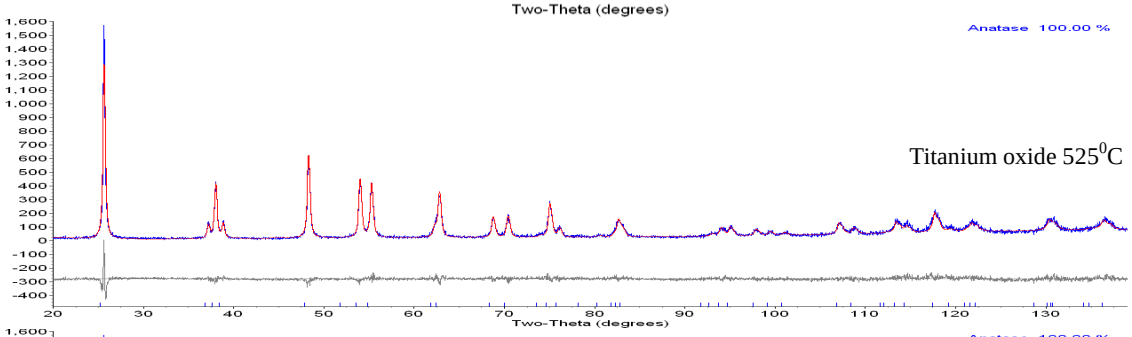
Anatase 100.00 %
Titanium oxide 525^{0}C
Two-Theta (degrees)

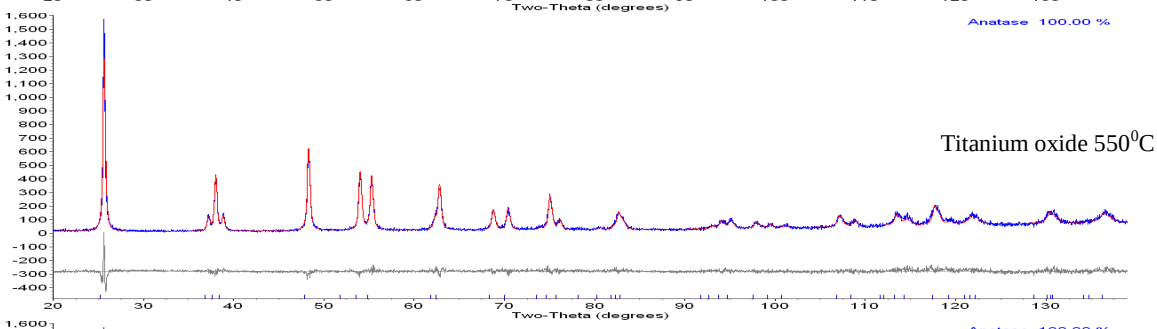
Anatase 100.00 %
Titanium oxide 550^{0}C
Two-Theta (degrees)

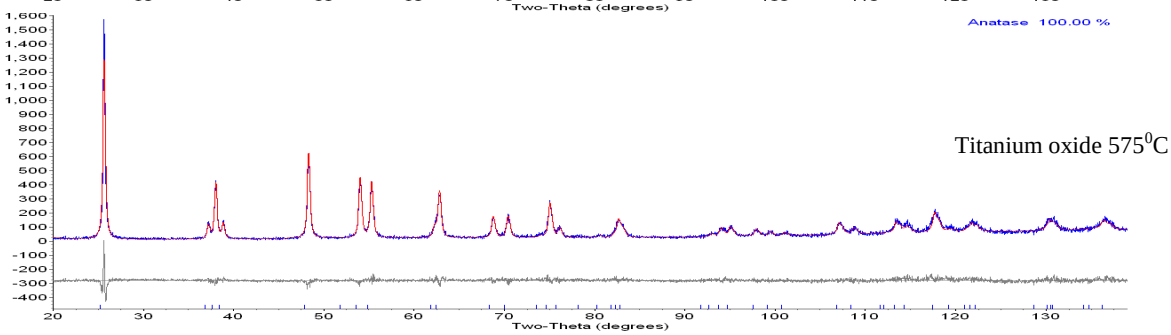
Anatase 100.00 %
Titanium oxide 575^{0}C
Two-Theta (degrees)

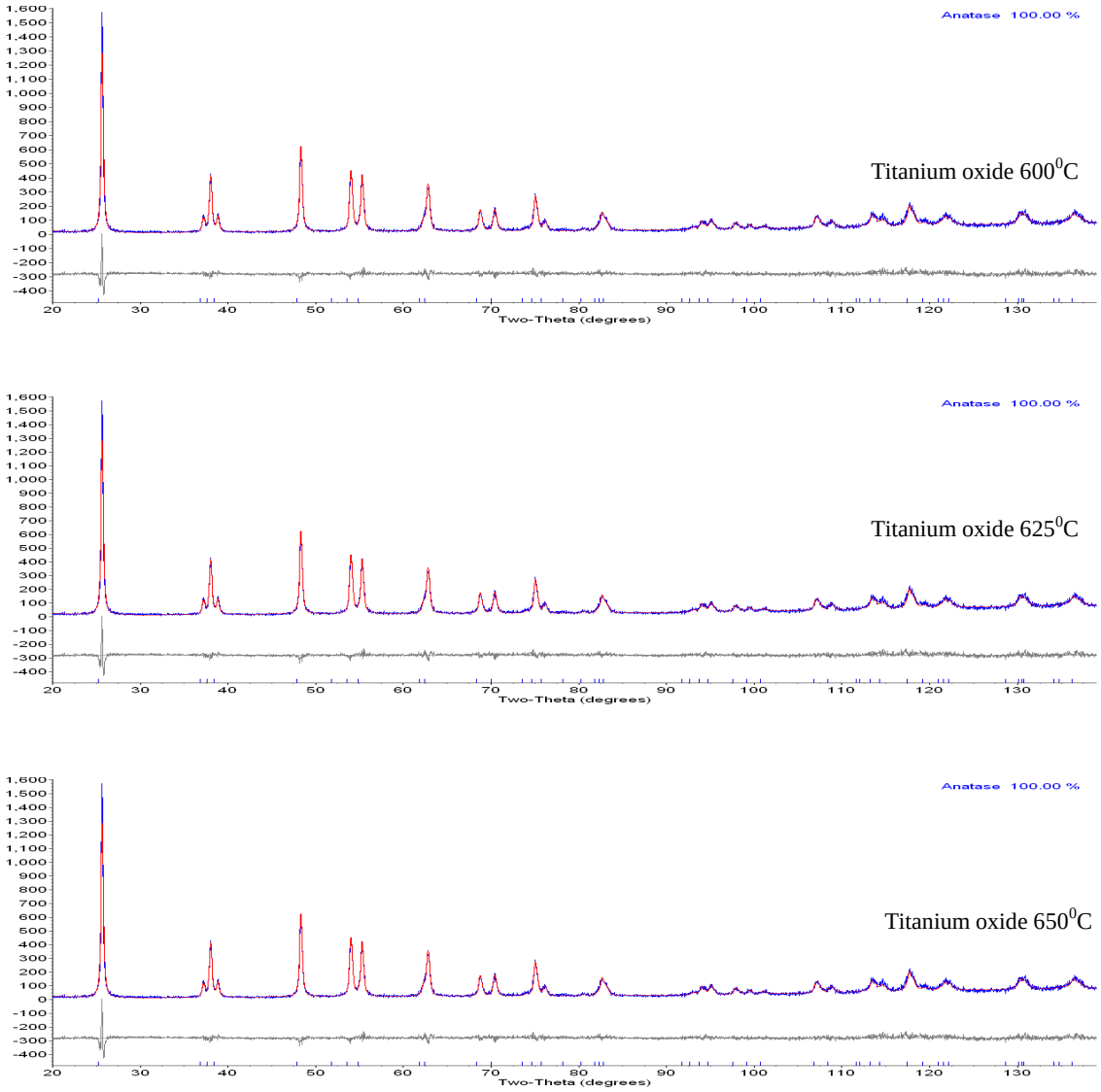

Figure 9. Refinement of titanium oxide powders as a function of heat-treatment temperature.

Table XI. Rietveld Derived Lattice Parameters, Cell Volumes and Goodness of Fits

Temperature (^{0}C)	a (Å)	b (Å)	C(Å)	Cell volume(Å^3)	R_{wp}
350^{0}C	3.7940(3)	3.7940(3)	9.5122(9)	136.92(2)	14.9
375^{0}C	3.7950(2)	3.7950(2)	9.5163(7)	137.05(2)	14.1
400^{0}C	3.7940(3)	3.7940(3)	9.5122(8)	136.92(2)	14.6
425^{0}C	3.7950(2)	3.7950(2)	9.5164(7)	137.05(2)	14.1
450^{0}C	3.7953(2)	3.7953(2)	9.5233(7)	137.17(2)	14.2
475^{0}C	3.7958(2)	3.7958(2)	9.5298(7)	137.31(2)	14.6
500^{0}C	3.7965(2)	3.7965(2)	9.5353(7)	137.43(2)	14.5
525^{0}C	3.7968(2)	3.7968(2)	9.5438(6)	137.58(2)	14.8
550^{0}C	3.7969(2)	3.7969(2)	9.5485(5)	137.65(1)	15.0
575^{0}C	3.7974(2)	3.7974(2)	9.5578(5)	137.82(1)	14.6
600^{0}C	3.7978(2)	3.7978(2)	9.5630(5)	137.93(1)	14.8
625^{0}C	3.7981(2)	3.7981(2)	9.5687(4)	138.03(1)	14.8
650^{0}C	3.7984(2)	3.7984(2)	9.5739(7)	138.13(1)	14.6

The Rietveld derived lattice parameters, cell volumes, and refined goodness of fits (defined as Rwp) are shown in Table XI. The errors estimated for each measurement are shown in the bracket (). The lattice parameters a and b are same as the crystal structure for anatase is tetragonal.

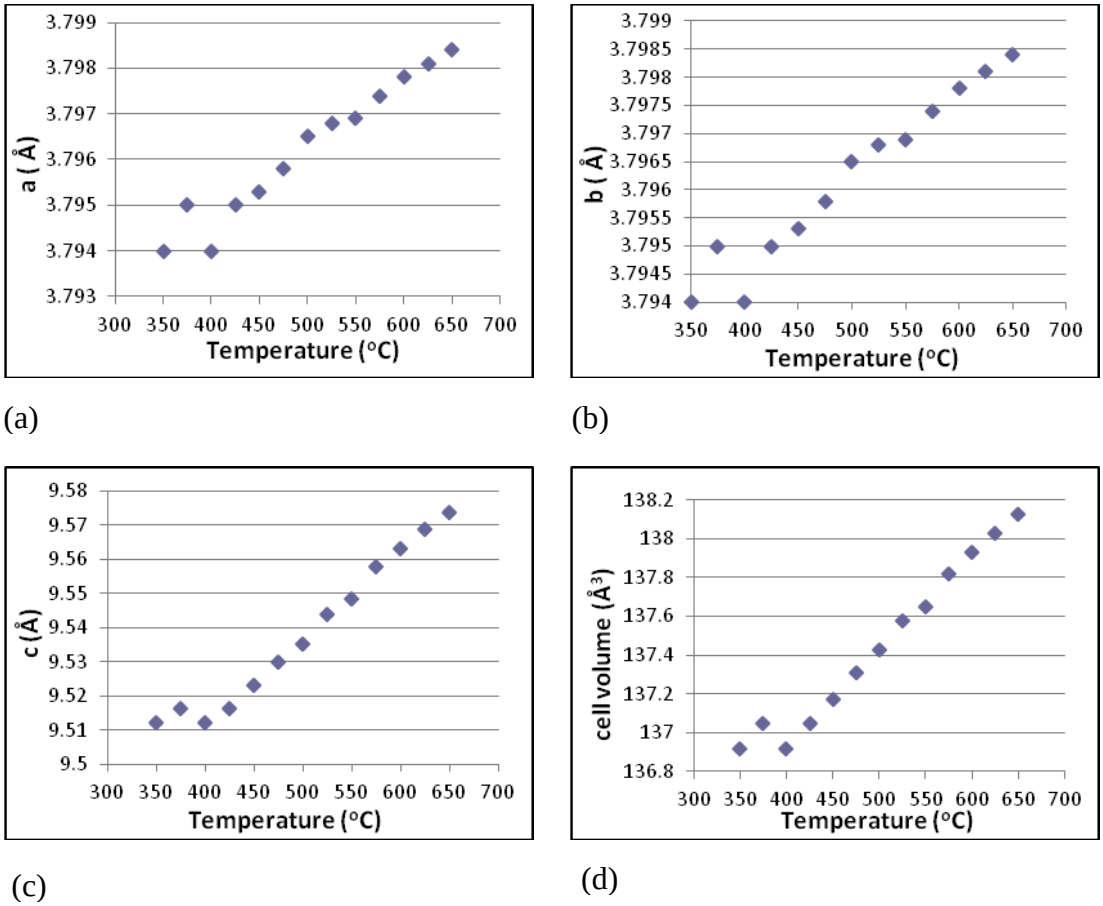

Figure 10. Refinement of titanium oxide powders as a function of heat-treatment temperature.

The graphs in Figure 10 shows change in lattice parameters and cell volume as a function of temperature. The lattice parameters (a, b and c) and cell volume increases from 350 – 375^{o}C and then drops from 375 – 400^{o}C. Above 400^{o}C the lattice parameters and cell volume shows continuous increase with temperature. The linear and volume expansion coefficients as a function of temperature were calculated by applying the same equations as in case of niobium oxide powders. Since a and b are same the linear thermal expansion coefficients (α_a and α_b) are also the same.

Table XII. Thermal Expansion Coefficients of Titanium Based Powders at Different Temperature

Temperature (^{0}C)	α_a (^{o}C^{-1}) (x10^{-6})	α_b(^{o}C^{-1}) (x10^{-6})	α_c (^{o}C^{-1}) (x10^{-6})	α_v (^{o}C^{-1}) (x10^{-6})
ti350	———	———	———	———
ti375	10.54	10.54	17.2	37.97
ti400	0	0	0	0
ti425	3.51	3.51	5.89	12.66
ti450	3.43	3.43	11.67	18.26
ti475	3.79	3.79	14.80	22.79
ti500	4.39	4.39	16.19	24.83
ti525	4.21	4.21	18.98	27.54
ti550	3.82	3.82	19.08	26.66
ti575	3.98	3.98	21.31	29.21
ti600	4.01	4.01	21.36	29.51
ti625	3.93	3.93	21.59	29.48
ti650	3.87	3.87	21.62	29.46

Table XII shows that linear thermal expansions (α_a, α_b and α_c) and volume expansion coefficients (α_v) are higher at 375^{o}C and then drops abruptly to zero at 400^{o}C.

The linear thermal expansion coefficients (α_a and α_b) increases from 400 to 425^{o}C and then slightly decrease at 450^{o}C. For 450-500^{o}C the values slightly increases again followed by decrease up to 550^{o}C. The linear thermal expansion (α_c) show rapid increase from 400-550^{o}C while the volume expansion (α_v) coefficients drops from 400 to 425^{o}C and then increases continuously from 450-550^{o}C. Above 550^{o}C the linear thermal expansions (α_a, α_b and α_c) and volume expansion coefficients (α_v) are nearly constant with slight variation of +/- 0.1 x10^{-6} ^{o}C^{-1}.

Table XIII. Crystallite Sizes as a Function of Temperature

Sample	Crystallite size (nm)
ti350	22(1)
ti375	23(1)
ti400	22(1)
ti425	23(1)
ti450	24(1)
ti475	26(1)
ti500	27(1)
ti525	30(1)
ti550	31(1)
ti575	35(1)
ti600	38(1)
ti625	41(1)
ti650	45(1)

Refined crystallite sizes of titanium based powders as a function of heat treatment are listed in Table XIII. The crystallite size of titanium oxide remains nearly constant at ~22nm for 350-425^{o}C. An increase in crystallite size is observed from 23 +/- 1 nm to 45 +/- 1 nm when titanium oxide powders are heated from 425 to 650^{o}C, respectively.

D. Raman spectroscopy

Raman spectroscopy was performed to determine the short-range structural changes in both niobium and titanium-based powders as a function of heat treatment temperature.

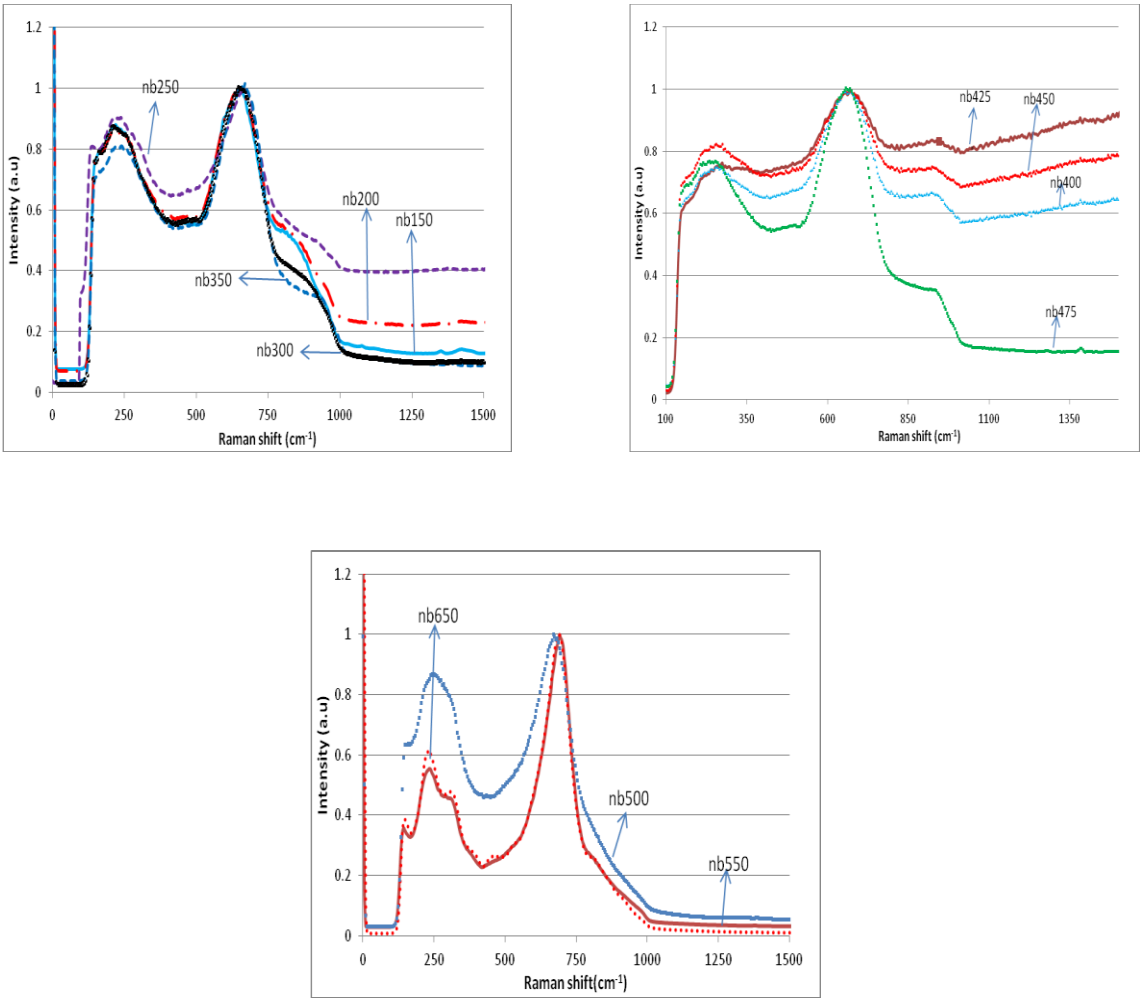

Figure 11. Raman Spectra for Niobium Oxide Heat treated to (a) 150 - 350°C (b) 400 - 475°C (c) 500 – 650°C.

Raman spectra for niobium samples heat treated from 150 to 650°C are shown in Figure 11 with approximate band positions listed in Table XIV and plotted Figure 12. In general, Raman spectra of niobium powders heat treated from 150 to 500°C show two broad bands at approximately 220 to 260 cm^{-1} and ~650 to 670 cm^{-1}. A shoulder on the high Raman shift side of the 650-670 cm^{-1} band (~800 to 900 cm^{-1}) is also

observed for niobium samples heated to between 150 and 500°C. A slight shoulder on the low Raman shift side of the 220-260 cm^{-1} band and weak bands at ~470 to 490 cm^{-1} are also observed. In comparison, niobium-based powders heat treated to 550 and 650°C exhibit well defined bands at ~147, 233, 452, and 691 cm^{-1} with shoulders observed at approximately 300 and 390 cm^{-1}.

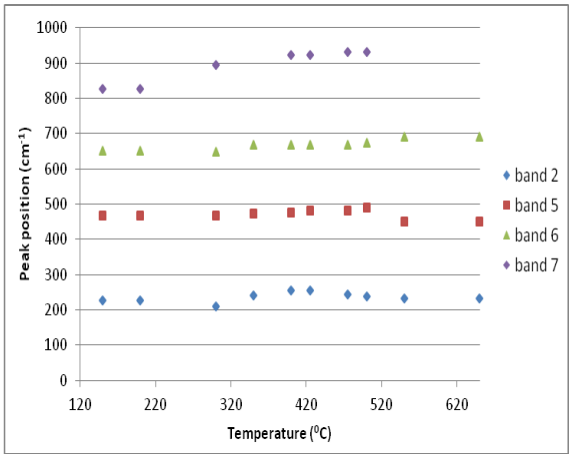

Figure 12. Variation in peak positions with temperature.

Table XIV. Raman Shifts (cm^{-1}) for Niobium Oxide Powders Heated at Different Temperatures

Temperature	Band#1	Band #2	Band# 3	Band# 4	Band #5	Band# 6	Band #7
150°C		227			469	652	827
200°C		227			469	652	827
300°C		210			469	648	894
350°C		238			491	670	923
400°C		256			482	670	923
425°C		256			482	670	923
450°C		256			482	670	932
475°C	147	243			478	670	932
500°C	147	242			474	674	
550°C		233	278	390	452	691	
650°C		233	305	390	452	691	

Table XV. Bands Assignment for Nb_2O_5

Bands	Assignments
Band #1	UA
Band #2	Banding of Nb-O-Nb
Band #3	UA
Band #4	UA
Band #5	UA
Band #6	Stretching of niobia polyhedra
Band #7	stretching of Nb=O

*****UA : unassigned

Table XV shows the assignment of different vibration modes to Raman bands for niobium-based powders heated from 150 to 650^{o}C based upon a number of previous studies[28,29]. The strong prominent band ~652 cm^{-1} is assigned to the symmetric stretching mode of niobia polyhedra. The weak band at ~890 cm^{-1} is due to symmetric stretching mode of Nb=O surface sites. The Raman band observed at lower frequencies around 233- 256 cm^{-1} was characteristic of the bending modes of Nb-O-Nb linkage.

The broad bands at temperatures between 150 – 475^{o}C suggest powders are amorphous[28]. The structure of amorphous phase is not well established but it was reported to contain slightly distorted NbO_6, NbO_7 and NbO_8 polyhedra[29]. The crystallization of powders to T-phase at 550^{o}C was evident from narrowing of broad peak and simultaneous shifting of bands from 670 to 691 cm^{-1} . Further, the absence of of band between 827 cm^{-1} - 932 cm^{-1} confirmed the presence of crystalline phase[28]. Even though the XRD pattern showed orthorhombic phase powders at 650^{o}C, it is difficult to distinguish the presence of T- from TT Nb_2O_5 as their Raman spectra looks similar[29]. This is consistent with the reports stating that the structures of T and TT phases are identical[28,30].

The heat treatment from 150 to 475^{o}C resulted in shifting of peaks at 652 cm^{-1} to 670 cm^{-1} which was accompanied by narrowing of the peak. The band at 827 cm^{-1} initially shifted to ~932 cm^{-1} and later disappeared.

At temperature above 500^{o}C crystallization into a hexagonal phase was apparent from the corresponding shift of the Raman band from 670 to ~692 cm^{-1} due to increase in bond order of niobia polyhedra and the sharpening of the band due to presence of more ordered structure. The single broad peak at low frequency ~256 cm^{-1} also formed four well defined peaks at ~147, 233, 278 and 290 cm^{-1}. The peak at 452 cm^{-1} became more prominent for powders heated at 650^{o}C. These are all consistent with crystallization of Nb_2O_5 [29].

The structural changes in the bonding environment of metal oxide with heat treatment resulted here in major shifts in Raman frequencies[29]. It has been reported that higher niobium-oxygen bond order shifted the Raman band to higher frequency which could be attributed to shorter bond length.[30]. This prominent shift upon crystallization has been demonstrated by broad peak for amorphous phase at ~660 cm^{-1} narrowing and shifting to 692cm^{-1} at higher temperature with simultaneous disappearance of weak band at ~890cm^{-1} which was present at low temperature[28].

Raman spectra shows (1) increase in signal intensity with increase in temperature (2) decrease in FWHM of peaks with increasing temperature which are features suggesting an increase in crystallite size[36].

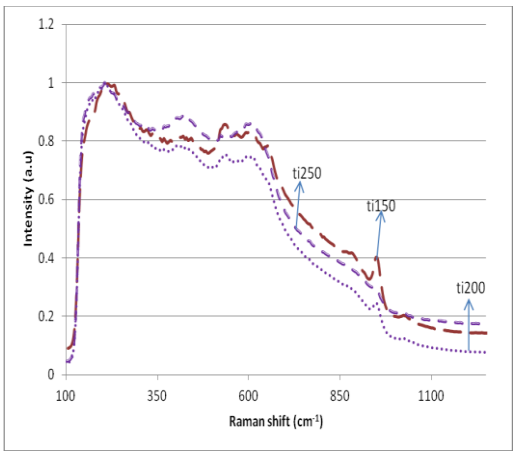

(a)

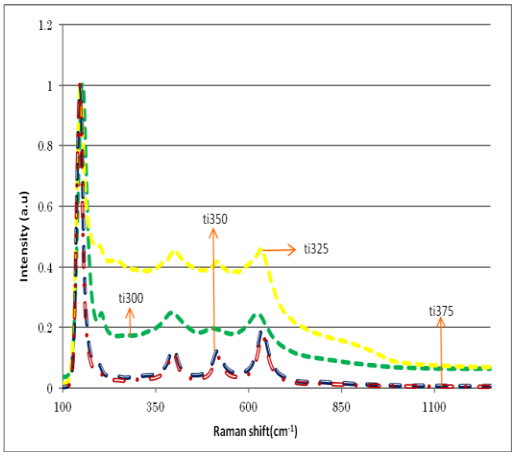

(b)

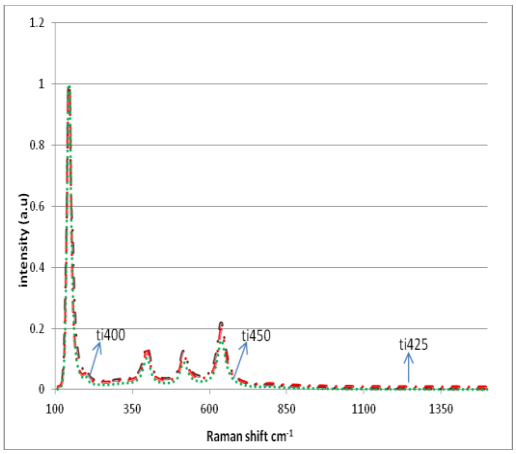

(c)

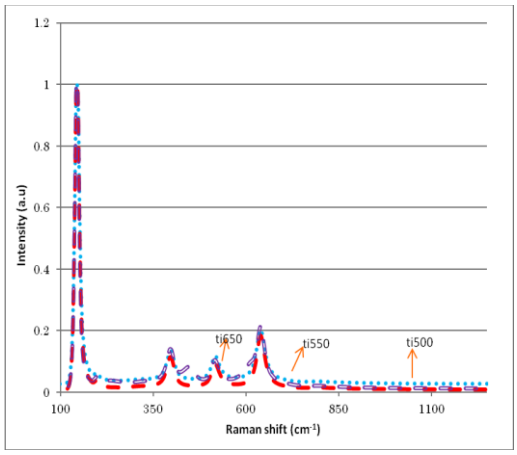

(d)

Figure 13. Raman spectra for titanium oxide heat treated to (a) 150 - 250^{o}C (b) 300 - 375^{o}C (c) 400 - 450^{o}C (d) 500 - 650^{o}C.

Raman spectra for titanium samples heat treated from 150 to 650^{o}C are shown in Figure 13 with approximate band positions listed in Table XVI and plotted in Figure 14. The powders heated at low temperatures 150^{o}C to 350^{o}C show broad peaks located at approximately 183 cm^{-1}, 206 cm^{-1}, ~425±5 cm^{-1}, 531 cm^{-1}, 605 cm^{-1} and 950 cm^{-1}. In general, Raman spectra of titanium powders heat treated from 350 to 650 ^{0}C shows five sharp, prominent peaks at approximately 147 cm^{-1}, 197cm^{-1}, 399 cm^{-1}, 518 cm^{-1} and 639 cm^{-1}. Band position as a function of temperature can be observed in Table XVI

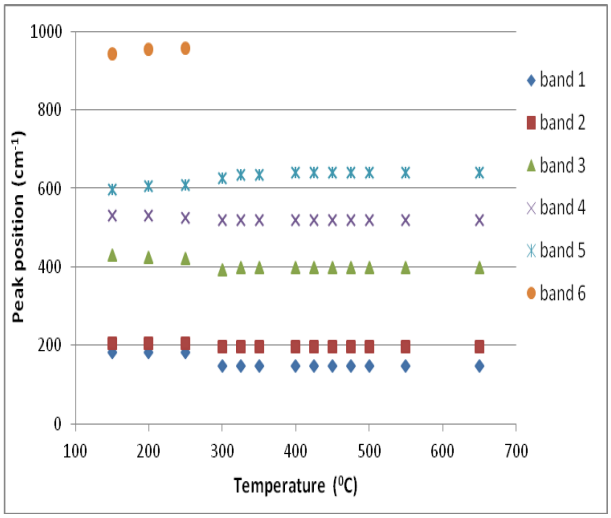

Figure 14. Variation in peak position with temperature.

Table XVI. Raman Shift (cm^{-1}) for Titanium Oxide Powders Heated at Different Temperatures

Temperature	Band# 1	Band# 2	Band# 3	Band# 4	Band# 5	Band# 6
150°C	183	206	430	531	596	944
200°C	183	206	425	531	605	953
250°C	183	206	421	526	609	957
300°C	147	197	394	518	626	
325°C	147	197	399	518	635	
350°C	147	197	399	518	635	
400°C	147	197	399	518	639	
425°C	147	197	399	518	639	
450°C	147	197	399	518	639	
475°C	147	197	399	518	639	
500°C	147	197	394	518	639	
550°C	147	197	394	518	639	
650°C	147	197	394	518	639	

Table XVII. Bands Assignment for TiO_2

Bands	Assignment
Band #1	O-Ti-O bending
Band #2	O-Ti-O bending
Band #3	O-Ti-O bending
Band #4	Ti-O stretching
Band #5	Ti-O stretching
Band #6	UA

*UA : unassigned

Table XVII shows the assignment of different vibration modes to Raman bands for titanium -based powders heated from 150^{o}C to 650^{o}C. The Raman spectra for titanium oxide heated from 150 – 325^{o}C showed broad and weak bands consistent with amorphous TiO_2[32]. An additional band at ~950 cm^{-1} was observed which disappeared at high temperature. This could be due to presence of adsorbed surface species eliminated at higher calcination temperature. The broadness of the peaks are a result of amorphous nature of the metal oxide at low temperatures and little strucutral information could be retrived by them. However, once the titanium oxide crystallized to anatase (>325^{o}C) prominent and sharp bands with stable positions at 147 cm^{-1} , 197 cm^{-1} , 394 cm^{-1} , 518 cm^{-1} and 639 cm^{-1} were observed. The first three modes corresponded to O-Ti-O stretching and the latter two bands to Ti-O stretching. The results are in good agreement with those found in literatures which also showed six Raman active fundamental modes at 144 cm^{-1} (E_g), 197 cm^{-1} (E_g), 397 cm^{-1} (B_{1g}), 518 cm^{-1} (A_{1g} and B_{1g} unresolved) and 640 cm^{-1} (E_g) for tetragonal anatase phase of titanium oxide.

It has been reported that distance between bands can provide information on the distortion of crystal structure. If the distance between A_{1g} + B_{1g} (518 cm^{-1}) and B_{1g} (399 cm^{-1}) is same as the distance between A_{1g} + B_{1g} (518 cm^{-1}) and E_g (639 cm^{-1}) then the structure is not distorted[62]. This respective distance was calculated to be 121 and 122 for temperature between 325 to 475^{o}C. At higher temperature, 500 to 650^{o}C the

respective distance was calculated as 124 and 122 respectively. This showed that at higher temperature (above 500^{o}C) the structure may be slightly distorted which could be due to thermal stress in the lattice.

It was reported for titanium oxide prepared by sulphate process for heat treatment from 300^{o}C to750^{o}C, Raman band at 144 cm^{-1} showed shift to lower frequency mode while B_{1g} at 396 cm^{-1} shifted to higher frequency[32]. This is slightly different to the results obtained for our samples as the Raman band at 147 cm^{-1} was constant and band at B_{1g} at 399 cm^{-1} shifted to lower frequency. Along with structural studies, it is also possible to estimate the ratio of different phases present from intensity calibration using standard mixtures[1,31]. The small variation in Raman peak positions could be due to error in instrument set up as the Rayleigh peak was not exactly centered to zero but was slightly towards right. The adjustments were made using software to reveal the band positions.

The results obtained from DTA, HTXRD, and Raman for niobium oxide as a function of heat-treatment are highly consistent with one another. However, for niobium-based powders we observed two important discrepencies (1) the XRD data showed hexagonal crystallization to occur at lower temperatures than expected from the DTA/TGA and (2) the phase transformation from hexagonal to orthorhombic phase at ~600^{o}C was observed only from HTXRD analysis. Furthermore, Raman analysis is also not sensitive to the differences in the hexagonal and orthorhombic phases.

The results obtained from DTA, HTXRD, and Raman for titanium oxide as a function of heat treatment are highly consistent with one another. However, again we observed two important discrepencies (1) the XRD data showed anatase crystallization to occur at lower temperatures than expected from the DTA/TGA and (2) DTA/TGA analyses suggested the anatase to rutile phase transformation occurs at a temperature below 600^{o}C, however, HTXRD analyses anatase was stable to 650^{o}C. The inconsistency in data obtained from high temperature XRD and DTA plots for both niobium and titanium oxides may be attributed to the differences in the heating schedule where 90 minutes dwell time was alloted for powders heated in situ for HTXRD while due to instrument restriction the powders in DTA was heated with no dwell time.

3. Bioactivity testing

A. Simulated Body Fluid (SBF) testing

Bioactivity testing was conducted on five selected samples having different crystal structure; TiO_2-amorphous, TiO_2-tetragonal, Nb_2O_5-amorphous, Nb_2O_5-hexagonal, and Nb_2O_5-orthorhombic. The samples were pressed into pellets and immersed in SBF for a period of 1, 7 and 30 days.

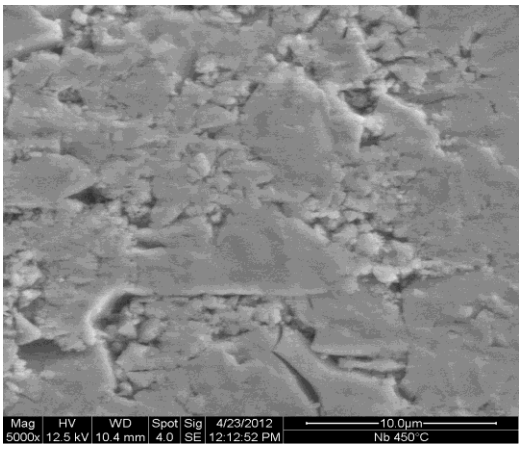

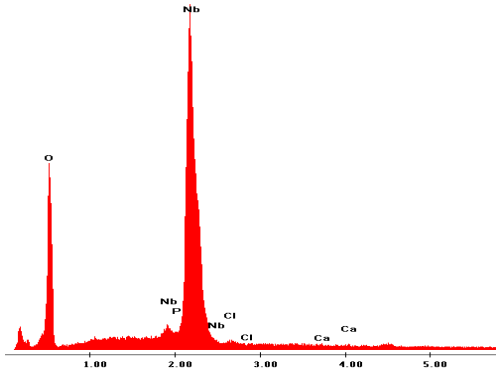

(a)

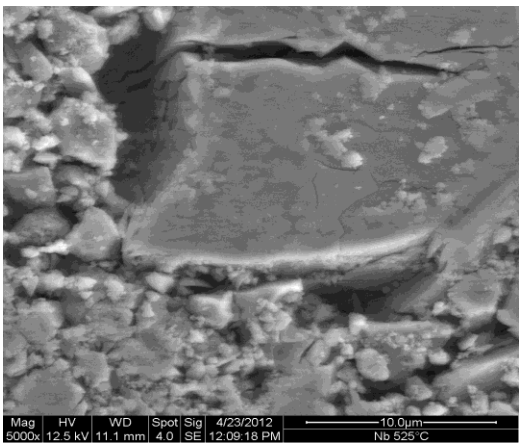

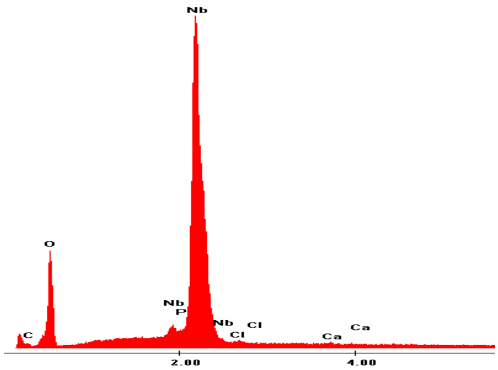

(b)

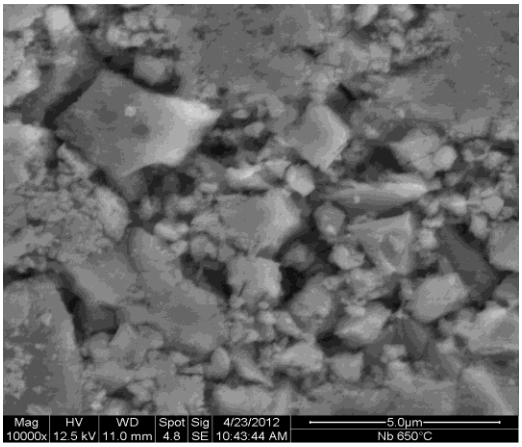

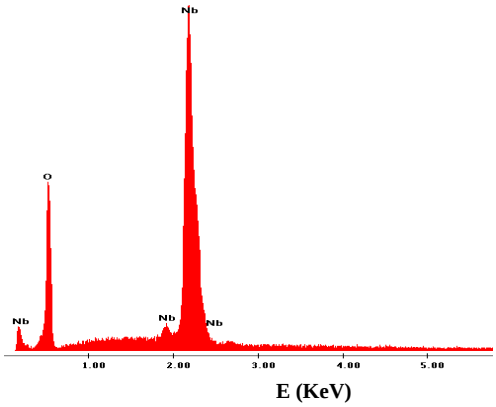

(c)

Figure 15. SEM and corresponding EDX spectra for 1day SBF immersed pellets of Nb_2O_5 a) amorphous b) hexagonal and c) orthorhombic at 5kx.

It is evident from Figure 15 (a), (b) and (c) that the surfaces of all samples do not show any Ca and P layer deposition after 1 day in SBF. The corresponding EDX analysis also does not show any significant peak for Ca or P.

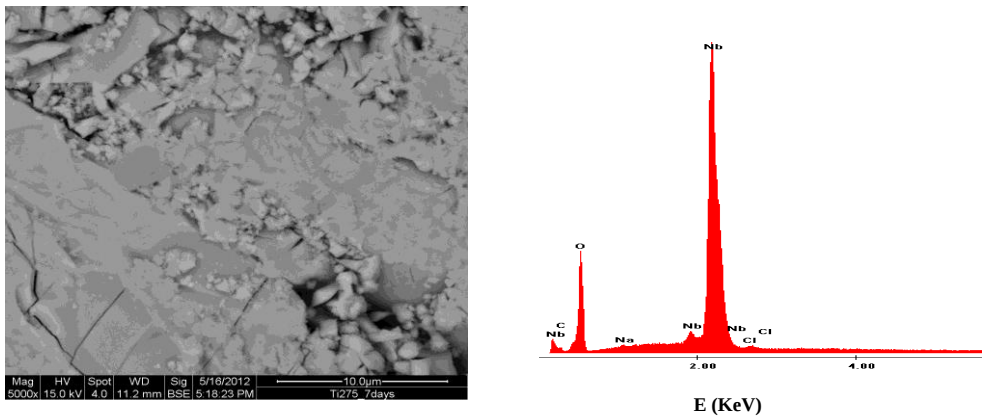

(a)

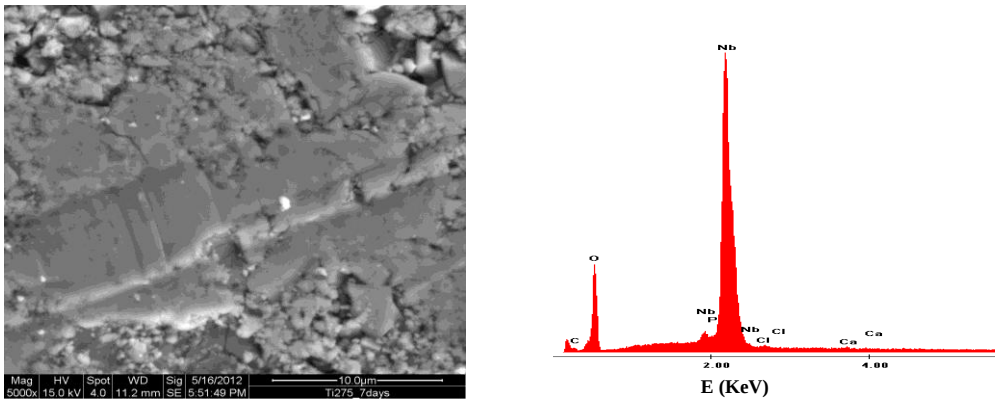

(b)

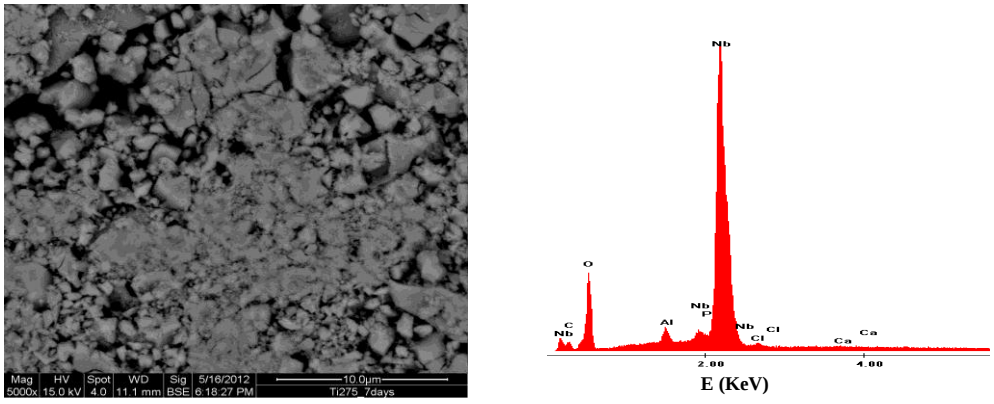

(c)

Figure 16. SEM images and corresponding EDX spectra for 7 days SBF immersed pellets of Nb_2O_5 a) amorphous b) hexagonal and c) orthorhombic at 5kx.

It is evident from Figure 16 (a), (b) and (c) that the surfaces of these oxides do not show any Ca and P layer deposition after 7 day in SBF. The corresponding EDX analysis also does not show any significant peak for Ca or P.

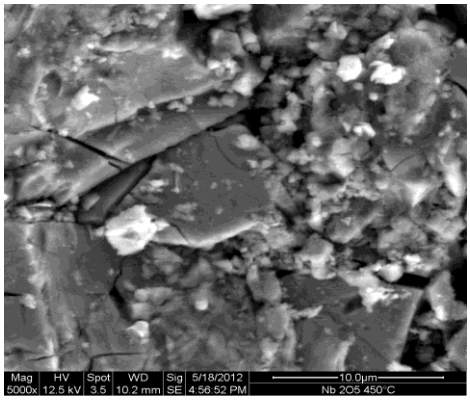

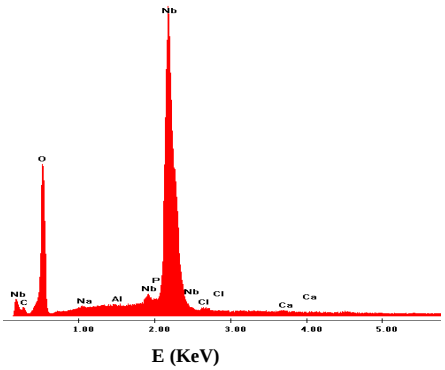

(a)

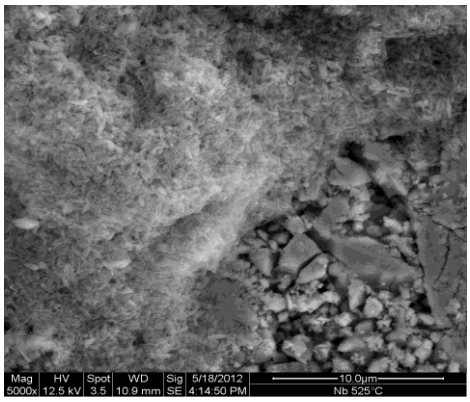

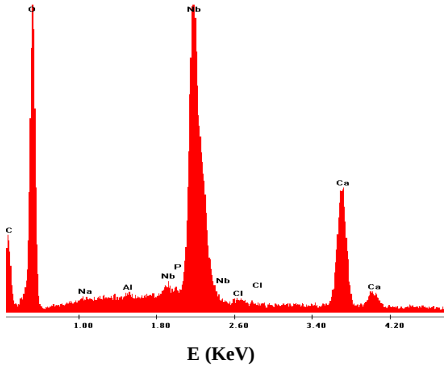

(b)

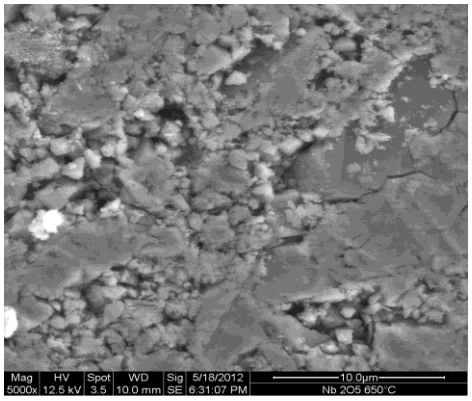

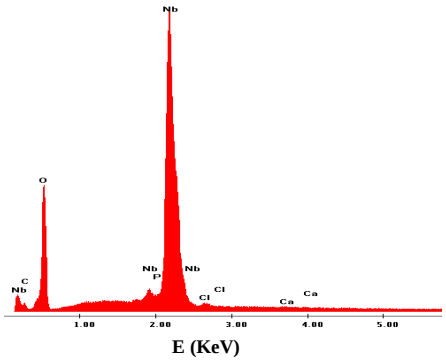

(c)

Figure 17. SEM images and corresponding EDX spectra for 30 days SBF immersed pellets of Nb_2O_5 a) amorphous b) hexagonal and c) orthorhombic at 5kx.

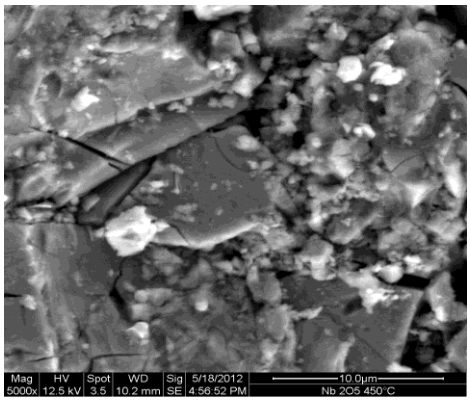

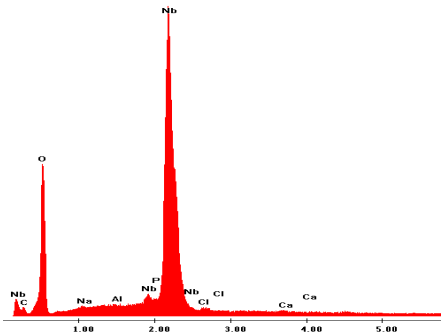

(a)

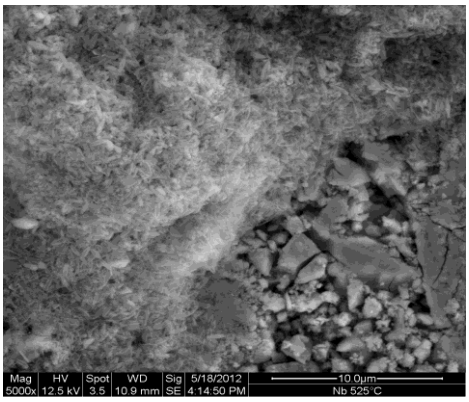

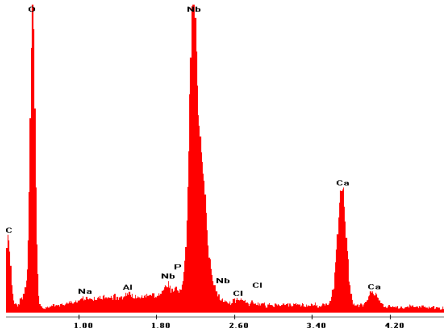

(b)

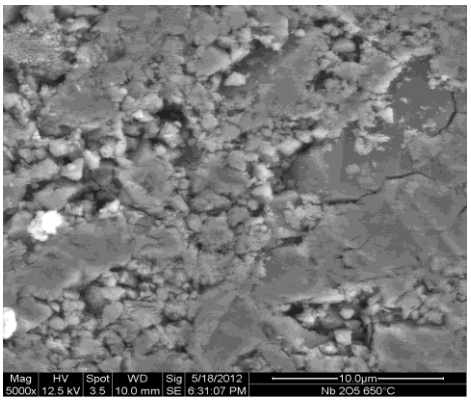

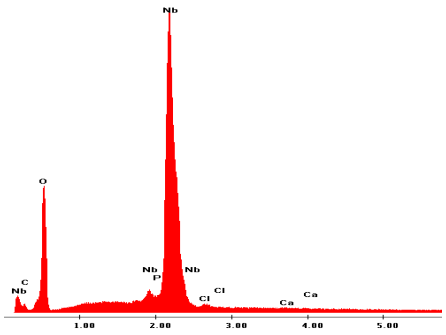

(c)

Figure 17 (a), (b) and (c) shows the SEM images for pellets after 30 days immersion in SBF. No Ca and P layer deposition at the oxide surface was observed for Nb_2O_5-amorphous or Nb_2O_5-orthorhombic. However, the Ca and P layer deposition at the

surface of Nb_2O_5-hexagonal was evident from the SEM images and was confirmed by the presence of Ca and P peaks in EDX analysis.

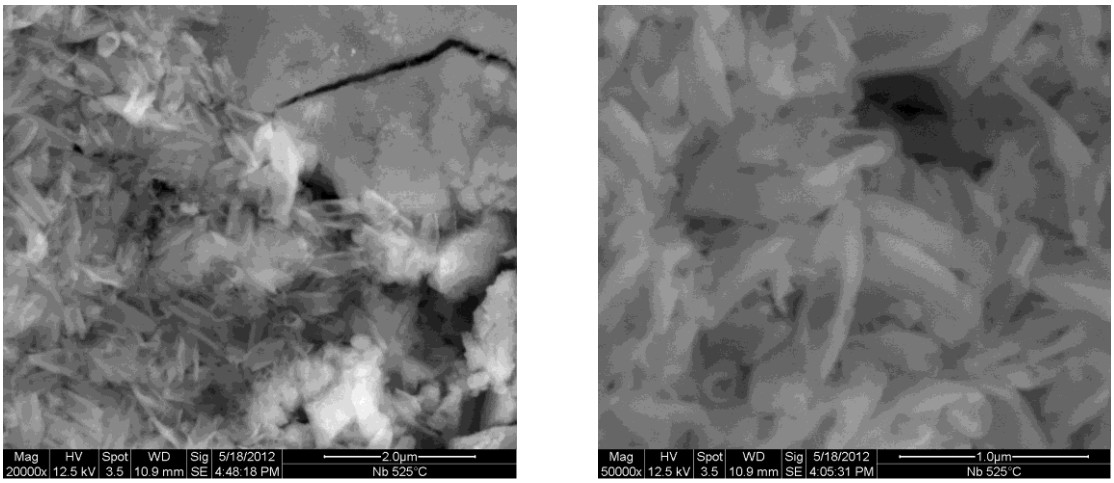

(a) (b)

Figure 18. SEM image of 30 days SBF immersed pellets of Nb_2O_5-hexagonal showing Ca and P layer at magnifications (a) 20kx (b) 50kx.

Figure 18 shows the high magnification SEM images of the Ca and P layer deposited at the surface of 30 days SBF immersed pellet of Nb_2O_5-hexagonal. At 20kx and 50 kx the morphology of Ca and P layer deposited appeared to be uniform and spiky in shape. The length of the particles was about ~1µm.

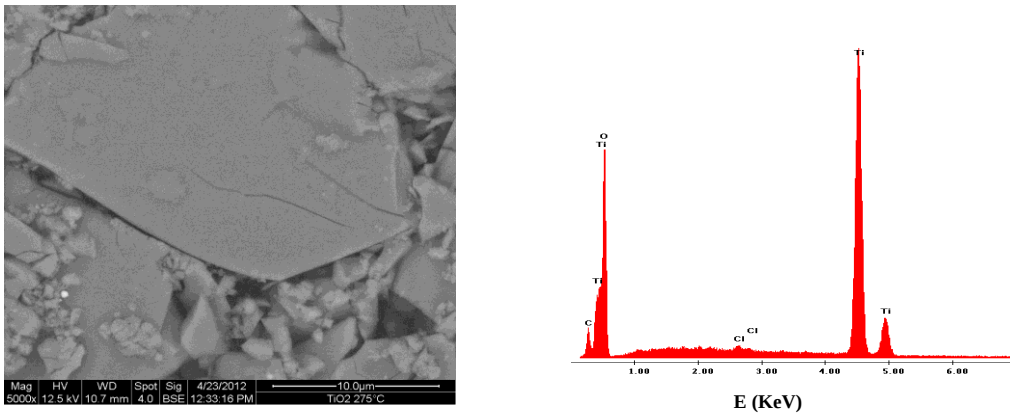

(a)

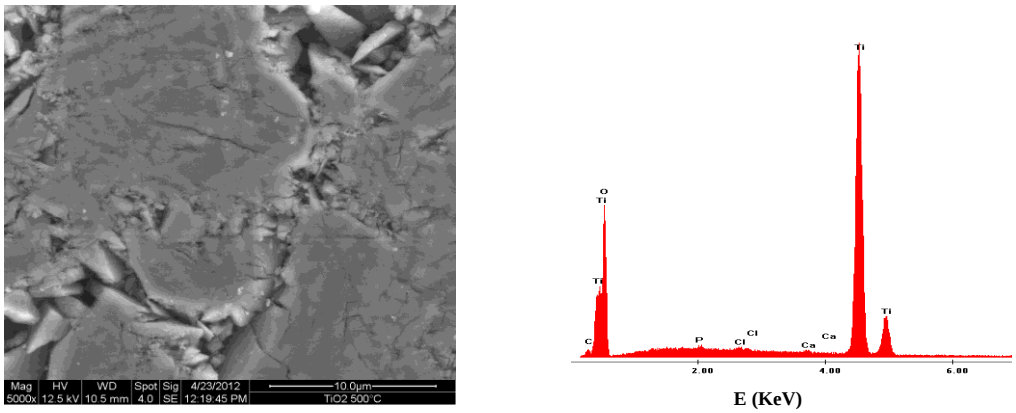

(b)

Figure 19. SEM images and corresponding EDX spectra for 1day SBF immersed pellets of TiO_2 a) amorphous b) tetragonal (anatase) at 5kx.

It is evident from Figure 19 that the surfaces of these oxides do not show any Ca and P layer deposition after 1 day in SBF. The corresponding EDX analysis also does not show any significant peak for Ca or P.

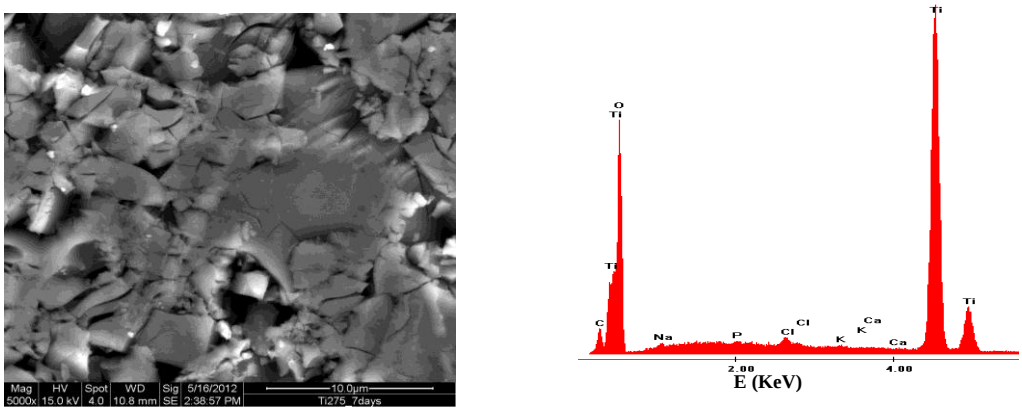

(a)

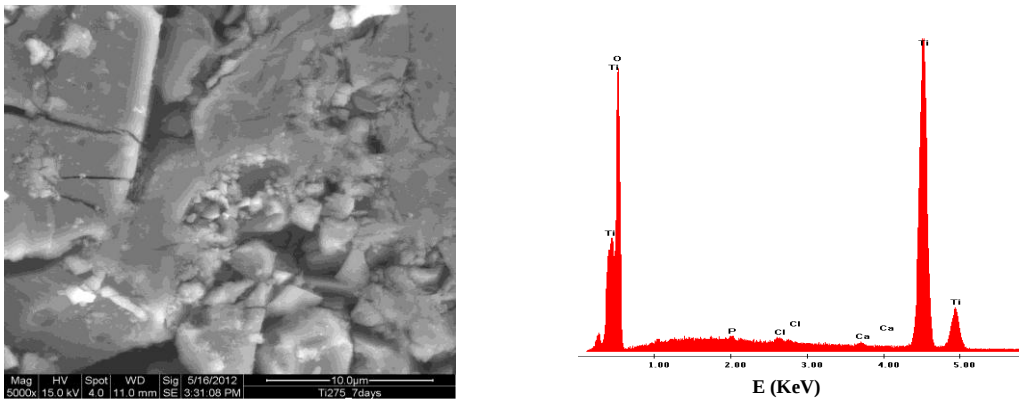

(b)

Figure 20. SEM images and corresponding EDX spectra for 7days SBF immersed pellets of TiO_2 a) amorphous b) tetragonal (anatase) at 5kx.

Figure 20 (a) and (b) shows that after 7 days immersion in SBF the deposition of Ca and P layer is not apparent from their SEM images. However, a small peak for Ca and P was observed for the EDX analysis of TiO_2-tetragonal (anatase) indicating the possible presence of Ca and P layer at the oxide surface. The TiO_2-amorphous did not show any Ca or P peaks via EDX analysis.

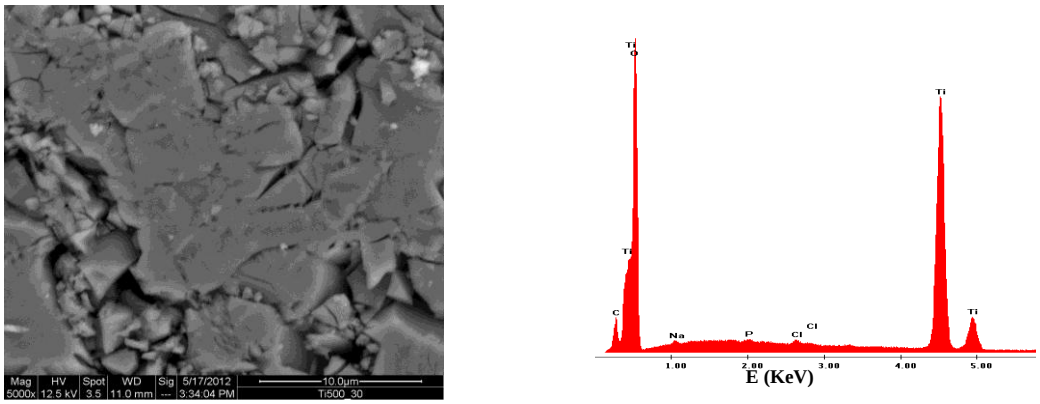

(a)

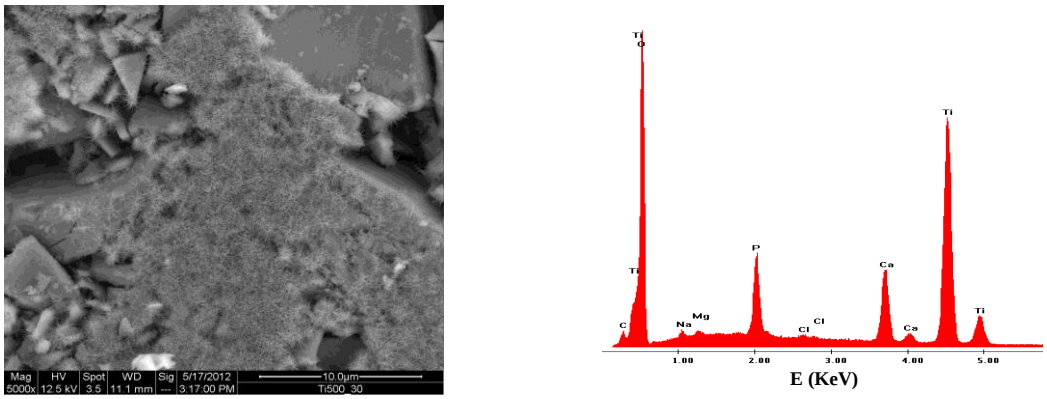

(b)

Figure 21. SEM images and corresponding EDX spectra for 30 days SBF immersed pellets of TiO_2 a) amorphous b) tetragonal (anatase) at 5kx.

Figure 21 (b) shows significant Ca and P layer deposition at the surface of TiO_2-tetragonal (anatase) after 30 days immersion in SBF. The presence of Ca and P peaks from EDX analysis confirmed their presence. Figure 21 (a) shows no Ca and P layer deposition at the surface of TiO_2-amorphous even after 30 days immersion in SBF. The absence of Ca and P peaks were also confirmed by EDX analysis.

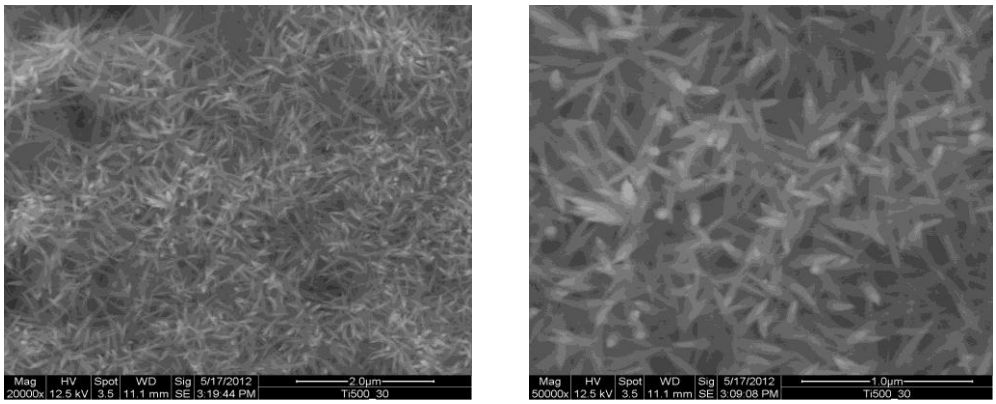

(a) (b)

Figure 22. SEM image of 30 days SBF immersed pellets of TiO_2-tetragonal (anatase) showing Ca and P layer deposition at magnifications (a) 20kx (b) 50kx.

Figure 22 shows the high magnification SEM images of the Ca and P layer deposited at the surface of 30 days SBF immersed pellet of TiO_2-tetragonal (anatase). At 20kx and 50 kx the morphology of Ca and P layer deposited appeared to be uniform and spiky in shape. The length of the particles was about ~1µm.

On comparing the Ca and P layer deposited at the surface of Nb_2O_5-hexagonal and TiO_2- tetragonal (anatase), it was observed that at the same magnification 50kx, the spiky particles appeared to be much smaller and sharper for TiO_2- tetragonal (anatase) than Nb_2O_5-hexagonal.

Simulated body fluid (SBF) testing was conducted on selected oxide composition and structures including; TiO_2-amorphous (275^oC), TiO_2-tetragonal (500 ^oC), Nb_2O_5-amorphous (450^oC), Nb_2O_5-hexagonal (525^oC), and Nb_2O_5-orthorhombic (650^oC). The pellets formed from the above compositions were immersed in SBF for 1, 7, and 30 days.

The SBF tested samples were observed under SEM for Ca and P layer deposition at the surface of pellets. The EDX analysis was conducted to confirm the presence of Ca and P layer deposited at the oxide surfaces.

The pellets obtained after 1 and 7 days did not show any Ca and P layer deposition. However the pellets immersed in SBF for 30 days showed Ca and P layer deposition for TiO_2 (anatase, 500^oC) and Nb_2O_5 (hexagonal, 525^oC).

The results are in agreement with the reports stating crystalline niobium oxide films prepared via sol-gel process by Eisenbarth et al. showed better results than amorphous niobium oxide[11]. Amorphous Nb_2O_5 pellets did not show any Ca and P layer deposition even when immersed in SBF for 30 days. On comparing, biocompatibility of amorphous niobium oxide prepared by sputtering technique with implant substrates (both Ti alloy and stainless steel) it was concluded that niobium oxide was beneficial for stainless steel substrates as it showed better biocompatibility along with surface mechanical property and corrosion resistance than stainless steel substrate[2]. However, the use of niobium coatings was not particularly helpful for substrates made of titanium alloys except for some improvement in corrosion resistance[4]. The structure and composition also plays an important role for biological responses. The crystalline niobium oxide films prepared via sol-gel process by Eisenbarth et.al showed better biological response than Ti alloys[9]. The presence of surface crystallinity and other properties induced by the structure was responsible for better results[9]. Surface roughness increases with increase in crystallite size. Hence amorphous niobium oxide is smoother than crystallized ones.

A comparative study of osteoblast responses of Nb_2O_5, TiO_2 and mixed oxide of SiO_2-TiO_2 prepared by sol-gel technique showed amorphous as prepared powders which remained so even after annealing at 450^oC except for TiO_2 which illustrated the presence of mixed (anatase and rutile) phase. The metal oxides were free of organic residue. The cytocompatibility analysis (non toxic effect induced by a biomaterial in cell-culture systems) gave best results for TiO_2 samples[3].

The biocompatibility of titanium oxide depends on crystal phase, particle size and degree of crystallinity. The results obtained by SBF analysis showed greater response for anatase TiO_2. This is in agreement with reports stating that apatite formation was greater for composites containing anatase phase rather than rutile phase of titanium oxide which shows that anatase is preferred phase for apatite formation[8].

The morphology of apatite formed at the metal oxide surface was found to be spike-like. In addition to Ca and P the EDX analysis showed the presence of Cl, Mg, Na which are coming out of the SBF solution. The morphologies of apatite formed may vary according to crystallinity, ratio of Ca and P and immersion period. This was demonstrated for TiO_2 prepared via sol-gel technique and heated at 300^oC which exhibited variation in morphology of the apatite formed at the surface from hair-like particles (after 1 day) to clustered ball-like particles (3-14 days). On comparing, the apatite formation was reported to be higher for samples heated at 300^oC (anatase, crystallite size ~11.25 nm) than at 700^oC (rutile, crystallite size ~39.46 nm) and unheated (amorphous). The presence of Ca and P was confirmed by XPS data which was supported by XRD data except for 1 day samples due to amorphous phase of apatite[7].

IV. CONCLUSION

Amorphous niobium and titanium oxides were successfully prepared via the sol-gel technique. The heat treatment from 150^0C to 650^oC resulted in different phases of metal oxides formed. The structural evolution and identification of phases were carried out using HTXRD complemented by Raman spectroscopy. Titanium oxide crystallized at low temperature (325^oC) to anatase. Anatase was stable and remained so until 650^oC. The niobium oxide initially crystallized into a hexagonal phase (500-525^oC) and then transformed to orthorhombic phase (550-650^oC). The structural changes in Raman were observed by narrowing and shifting of peaks when the oxide approached crystallization. The biocompatibility analysis conducted using SBF testing concluded that Ca and P layer deposition was favorable for anatase TiO_2 and hexagonal Nb_2O_5. The other factors such as high organic content, presence of contamination, higher density could also be responsible for no Ca and P layer deposition on other oxides.

V. FUTURE WORK

- GIXRD (Grazing Incidence X-Ray diffraction) to determine whether the Ca and P layer deposited at the oxide surface was crystalline or amorphous.
- Perform cell cytotoxicity analysis using standard mouse fibroblast cells
- Perform porosity analysis on samples
- Determine the presence of organic residue by carbon analyzer or mass spectroscopy
- Prepare sol-gel thin films on metallic substrate or glass

REFERENCES

1. T.D. Robert, L.D. Laude, V.M. Geskin, R. Lazzaroni, and R. Gouttebaron, "Micro-Raman spectroscopy study of surface transformations induced by excimer laser irradiation of TiO2," *Thin Solid Films,* **440** [1–2] 268-77 (2003).

2. G. Ramírez, S.E. Rodil, S. Muhl, D. Turcio-Ortega, J.J. Olaya, M. Rivera, E. Camps, and L. Escobar-Alarcón, "Amorphous niobium oxide thin films," *J. Non-Cryst. Solids,* **356** [50–51] 2714-21 (2010).

3. A. Ochsenbein, F. Chai, S. Winter, M. Traisnel, J. Breme, and H.F. Hildebrand, "Osteoblast responses to different oxide coatings produced by the sol–gel process on titanium substrates," *Acta Biomater.,* **4** [5] 1506-17 (2008).

4. G. Ramírez, S.E. Rodil, H. Arzate, S. Muhl, and J.J. Olaya, "Niobium based coatings for dental implants," *Appl. Surf. Sci.,* **257** [7] 2555-9 (2011).

5. X.-m. Cheng, B.-m. Nie, and S. Kumar, "Preparation and bioactivity of SiO2 functional films on titanium by PACVD," *Trans. Nonferrous Metals Soc. China,* **18** [3] 627-30 (2008).

6. Y. Han, D. Chen, J. Sun, Y. Zhang, and K. Xu, "UV-enhanced bioactivity and cell response of micro-arc oxidized titania coatings," *Acta Biomater.,* **4** [5] 1518-29 (2008).

7. C.-M. Lin and S.-K. Yen, "Biomimetic growth of apatite on electrolytic TiO2 coatings in simulated body fluid," *Mater.s Sci. Eng.: C,* **26** [1] 54-64 (2006).

8. H. Maeda, T. Kasuga, and M. Nogami, "Apatite formation on titania–vaterite powders in simulated body fluid," *J. Euro.n Cera. Soc.,* **24** [7] 2125-30 (2004).

9. E. Eisenbarth, D. Velten, M. Müller, R. Thull, and J. Breme, "Nanostructured niobium oxide coatings influence osteoblast adhesion," *J. Biomed. Mater. Res. Part A,* **79A** [1] 166-75 (2006).

10. W.J. Nascimento, T.G.M. Bonadio, V.F. Freitas, W.R. Weinand, M.L. Baesso, and W.M. Lima, "Nanostructured Nb2O5–natural hydroxyapatite formed by the mechanical alloying method: A bulk composite," *Mater. Chem. Phys.,* **130** [1–2] 84-9 (2011).

11. R. Olivares-Navarrete, J.J. Olaya, C. Ramírez, and S.E. Rodil, "Biocompatibility of Niobium Coatings," *Coatings,* **1** [1] 72-87 (2011).

12. M. Kalbacova, J.M. Macak, F. Schmidt-Stein, C.T. Mierke, and P. Schmuki, "TiO2 nanotubes: photocatalyst for cancer cell killing," *physica status solidi (RRL) – Rapid Research Letters,* **2** [4] 194-6 (2008).

13. A. Nakajima, K. Takakuwa, Y. Kameshima, M. Hagiwara, S. Sato, Y. Yamamoto, N. Yoshida, T. Watanabe, and K. Okada, "Preparation and properties of titania–apatite hybrid films," *J. Photochem. Photobio. A:,* **177** [1] 94-9 (2006).

14. T. Kaneko, M. Fujii, T. Kodama, and Y. Kitayama, "Synthesis of Titania Pillared Mica in Aqueous Solution of Acetic Acid," *J. Porous Materials,* **8** [2] 99-109 (2001).

15. J. Keleher, J. Bashant, N. Heldt, L. Johnson, and Y. Li, "Photo-catalytic preparation of silver-coated TiO₂ particles for antibacterial applications," *World J. Microbio. Biotechnolo,* **18** [2] 133-9 (2002).

16. T. Kokubo and H. Takadama, "How useful is SBF in predicting in vivo bone bioactivity?," *Biomaterials,* **27** [15] 2907-15 (2006).

17. A. Oyane, H.-M. Kim, T. Furuya, T. Kokubo, T. Miyazaki, and T. Nakamura, "Preparation and assessment of revised simulated body fluids," *J. Biomed Mater. Res. Part A,* **65A** [2] 188-95 (2003).

18. A. Cüneyt Tas, "Synthesis of biomimetic Ca-hydroxyapatite powders at 37°C in synthetic body fluids," *Biomaterials,* **21** [14] 1429-38 (2000).

19. T. Kokubo, "Design of bioactive bone substitutes based on biomineralization process," *Mater. Sci. Eng: C,* **25** [2] 97-104 (2005).

20. E.-S. Ghaith, T. Hayakawa, T. Kasuga, and M. Nogami, "Apatite formation on CO2 laser irradiated titanium oxide films," *Mater. Lett.,* **60** [2] 194-7 (2006).

21. M.G. Faga, A. Vallée, A. Bellosi, M. Mazzocchi, N.N. Thinh, G. Martra, and S. Coluccia, "Chemical treatment on alumina–zirconia composites inducing apatite formation with maintained mechanical properties," *J. Euro. Cera. Soc,* **32** [10] 2113-20 (2012).

22. T. Kokubo, T. Matsushita, H. Takadama, and T. Kizuki, "Development of bioactive materials based on surface chemistry," *J. Euro. Cera. Soc,* **29** [7] 1267-74 (2009).

23. J.M. Wörle-Knirsch, K. Kern, C. Schleh, C. Adelhelm, C. Feldmann, and H.F. Krug, "Nanoparticulate Vanadium Oxide Potentiated Vanadium Toxicity in Human Lung Cells," *Environm. Science & Technology,* **41** [1] 331-6 (2006).

24. F. Liang, L. Zhou, and K. Wang, "Apatite formation on porous titanium by alkali and heat-treatment," *Surf. Coat.Technolo.,* **165** [2] 133-9 (2003).

25. M. Keshmiri and T. Troczynski, "Apatite formation on TiO2 anatase microspheres," *J. Non-Cryst. Solids,* **324** [3] 289-94 (2003).

26. Y.-F. Zheng, H.-Z. Liu, Z.-J. Liu, and X.-N. Li, "In situ X-ray diffraction study of reduction processes of Fe3O4- and Fe1−xO-based ammonia-synthesis catalysts," *J. Solid State Chem.,* **182** [9] 2385-91 (2009).

27. M. Halvarsson, V. Langer, and S. Vuorinen, "Determination of the thermal expansion of κ-Al2O3 by high temperature XRD," *Surf. Coat. Technolo.,* **76–77, Part 1** [0] 358-62 (1995).

28. R.M. Pittman and A.T. Bell, "Raman studies of the structure of niobium oxide/titanium oxide (Nb2O5.TiO2)," *The Journal of Physical Chemistry,* **97** [47] 12178-85 (1993).

29. J.M. Jehng and I.E. Wachs, "ChemInform Abstract: Structural Chemistry and Raman Spectra of Niobium Oxides," *ChemInform,* **22** [15] no-no (1991).

30. B.X. Huang, K. Wang, J.S. Church, and Y.-S. Li, "Characterization of oxides on niobium by raman and infrared spectroscopy," *Electrochimica Acta,* **44** [15] 2571-7 (1999).

31. L.J. Hardwick, M. Holzapfel, P. Novák, L. Dupont, and E. Baudrin, "Electrochemical lithium insertion into anatase-type TiO2: An in situ Raman microscopy investigation," *Electrochimica Acta,* **52** [17] 5357-67 (2007).

32. N. Mahdjoub, N. Allen, P. Kelly, and V. Vishnyakov, "SEM and Raman study of thermally treated TiO2 anatase nanopowders: Influence of calcination on photocatalytic activity," *Journal of Photochemistry and Photobiology A: Chemistry,* **211** [1] 59-64 (2010).

33. C. Alquier, M.T. Vandenborre, and M. Henry, "Synthesis of niobium pentoxide gels," *Journal of Non-Crystalline Solids,* **79** [3] 383-95 (1986).

34. M.A. Aegerter, C.O. Avellaneda, A. Pawlicka, and M. Atik, "Electrochromism in Materials Prepared by the Sol-Gel Process," *Journal of Sol-Gel Science and Technology,* **8** [1] 689-96 (1997).

35. B. Prasai, B. Cai, M. Underwood, J. Lewis, and D. Drabold, "Properties of amorphous and crystalline titanium dioxide from first principles," *J. Mater. Sci,* 1-7.

36. A. Orendorz, A. Brodyanski, J. Lösch, L.H. Bai, Z.H. Chen, Y.K. Le, C. Ziegler, and H. Gnaser, "Structural transformations in nanocrystalline anatase TiO2 films upon annealing in air," *Surf. Sci.,* **600** [18] 4347-51 (2006).

37. I.A. Alhomoudi and G. Newaz, "Residual stresses and Raman shift relation in anatase TiO2 thin film," *Thin Solid Films,* **517** [15] 4372-8 (2009).

38. G.-R. Gu, Y.-A. Li, Y.-C. Tao, Z. He, J.-J. Li, H. Yin, W.-Q. Li, and Y.-N. Zhao, "Investigation on the structure of TiO2 films sputtered on alloy substrates," *Vacuum,* **71** [4] 487-90 (2003).

39. S.H. Mujawar, A.I. Inamdar, S.B. Patil, and P.S. Patil, "Electrochromic properties of spray-deposited niobium oxide thin films," *Solid State Ionics,* **177** [37–38] 3333-8 (2006).

40. P.S. Patil, R.K. Kawar, and S.B. Sadale, "Electrochromism in spray deposited iridium oxide thin films," *Electrochimica Acta,* **50** [12] 2527-32 (2005).

41. M. Ristić, S. Popović, and S. Musić, "Sol–gel synthesis and characterization of Nb2O5 powders," *Materials Letters,* **58** [21] 2658-63 (2004).

42. B. Ohtani, K. Iwai, S.-i. Nishimoto, and T. Inui, "Electrochromism of Niobium Oxide Thin Films Prepared by the Sol-Gel Process," *Journal of The Electrochemical Society,* **141** [9] 2439-42 (1994).

43. R. Parra, M.S. Góes, M.S. Castro, E. Longo, P.R. Bueno, and J.A. Varela, "Reaction Pathway to the Synthesis of Anatase via the Chemical Modification of Titanium Isopropoxide with Acetic Acid," *Chem. Mater.,* **20** [1] 143-50 (2007).

44. N. Özer, "Optical and electrochemical characteristics of sol-gel deposited tungsten oxide films: a comparison," *Thin Solid Films,* **304** [1–2] 310-4 (1997).

45. D.A.B. de Filho, D.W. Franco, P.P.A. Filho, and O.L. Alves, "Niobia films: surface morphology, surface analysis, photoelectrochemical properties and crystallization process," *J. Mater. Sci.,* **33** [10] 2607-16 (1998).

46. A. Pawlicka, M. Atik, and M.A. Aegerter, "Synthesis of multicolor Nb2O5 coatings for electrochromic devices," *Thin Solid Films,* **301** [1–2] 236-41 (1997).

47. M. Schmitt, S. Heusing, M.A. Aegerter, A. Pawlicka, and C. Avellaneda, "Electrochromic properties of Nb2O5 sol–gel coatings," *Solar Energy Materials and Solar Cells,* **54** [1–4] 9-17 (1998).

48. M. Maček and B. Orel, "Electrochromism of sol–gel derived niobium oxide films," *Solar Energy Materials and Solar Cells,* **54** [1–4] 121-30 (1998).

49. A.V. Rosario and E.C. Pereira, "Lithium insertion in TiO2 doped Nb2O5 electrochromic thin films," *Electrochimica Acta,* **46** [12] 1905-10 (2001).

50. J. Livage and D. Ganguli, "Sol–gel electrochromic coatings and devices: A review," *Solar Energy Materials and Solar Cells,* **68** [3–4] 365-81 (2001).

51. T. Yoko, L. Hu, H. Kozuka, and S. Sakka, "Photoelectrochemical properties of TiO2 coating films prepared using different solvents by the sol-gel method," *Thin Solid Films,* **283** [1–2] 188-95 (1996).

52. M.C. Advincula, F.G. Rahemtulla, R.C. Advincula, E.T. Ada, J.E. Lemons, and S.L. Bellis, "Osteoblast adhesion and matrix mineralization on sol–gel-derived titanium oxide," *Biomaterials,* **27** [10] 2201-12 (2006).

53. S.-S. Hong, M.S. Lee, S.S. Park, and G.-D. Lee, "Synthesis of nanosized TiO2/SiO2 particles in the microemulsion and their photocatalytic activity on the decomposition of p-nitrophenol," *Catalysis Today,* **87** [1–4] 99-105 (2003).

54. X.-X. Wang, W. Yan, S. Hayakawa, K. Tsuru, and A. Osaka, "Apatite deposition on thermally and anodically oxidized titanium surfaces in a simulated body fluid," *Biomaterials,* **24** [25] 4631-7 (2003).

55. S.B. Deshpande, H.S. Potdar, Y.B. Khollam, K.R. Patil, R. Pasricha, and N.E. Jacob, "Room temperature synthesis of mesoporous aggregates of anatase TiO2 nanoparticles," *Mater. Chem. Phys,* **97** [2–3] 207-12 (2006).

56. M.R. Mohammadi, D.J. Fray, and A. Mohammadi, "Sol–gel nanostructured titanium dioxide: Controlling the crystal structure, crystallite size, phase transformation, packing and ordering," *Microporous and Mesoporous Mater,* **112** [1–3] 392-402 (2008).

57. R.S. Sonawane, S.G. Hegde, and M.K. Dongare, "Preparation of titanium(IV) oxide thin film photocatalyst by sol–gel dip coating," *Mater.Chem Phys,* **77** [3] 744-50 (2003).

58. K. Yoshimura, T. Miki, S. Iwama, and S. Tanemura, "Characterization of niobium oxide electrochromic thin films prepared by reactive d.c. magnetron sputtering," *Thin Solid Films,* **281–282** [0] 235-8 (1996).

59. N. Özer, D.-G. Chen, and C.M. Lampert, "Preparation and properties of spin-coated Nb2O5 films by the sol-gel process for electrochromic applications," *Thin Solid Films,* **277** [1–2] 162-8 (1996).

60. H. Zhang and J.F. Banfield, "Kinetics of Crystallization and Crystal Growth of Nanocrystalline Anatase in Nanometer-Sized Amorphous Titania," *Chem. Mater,* **14** [10] 4145-54 (2002).

61. D.J. Kim, S.H. Hahn, S.H. Oh, and E.J. Kim, "Influence of calcination temperature on structural and optical properties of TiO2 thin films prepared by sol–gel dip coating," *Materials Letters,* **57** [2] 355-60 (2002).

62. W.-X. Xu, S. Zhu, X.-C. Fu, and Q. Chen, "The structure of TiOx thin film studied by Raman spectroscopy and XRD," *Appl. Surf. Sci.* **148** [3–4] 253-62 (1999).

66. S.B. Deshpande, H.S. Potdar, Y.B. Khollam, K.R. Patil, R. Pasricha, and N.E. Jacob, "Room temperature synthesis of mesoporous aggregates of anatase TiO2 nanoparticles," *Mater. Chem. Phys.*, 97 [2–3] 207-12 (2006).

67. A. Pawlicka, M. Atik, and M.A. Aegerter, "Synthesis of multicolor Nb2O5 coatings for electrochromic devices," *Thin Solid Films,* 301 [1–2] 236-41 (1997).

68. M. Schmitt, S. Heusing, M.A. Aegerter, A. Pawlicka, and C. Avellaneda, "Electrochromic properties of Nb2O5 sol–gel coatings," *Solar Energy Materials and Solar Cells,* 54 [1–4] 9-17 (1998).

69. B. Ohtani, K. Iwai, S.-i. Nishimoto, and T. Inui, "Electrochromism of Niobium Oxide Thin Films Prepared by the Sol-Gel Process," *J. Electrochemical Society,* 141 [9] 2439-42 (1994).

70. M. Ristić, S. Popović, and S. Musić, "Sol–gel synthesis and characterization of Nb2O5 powders," *Materials Letters,* 58 [21] 2658-63 (2004).

71. M.R. Mohammadi, D.J. Fray, and A. Mohammadi, "Sol–gel nanostructured titanium dioxide: Controlling the crystal structure, crystallite size, phase transformation, packing and ordering," *Microporous and Mesoporous Materials,* 112 [1–3] 392-402 (2008).

72. S.-S. Hong, M.S. Lee, S.S. Park, and G.-D. Lee, "Synthesis of nanosized TiO2/SiO2 particles in the microemulsion and their photocatalytic activity on the decomposition of p-nitrophenol," *Catalysis Today,* 87 [1–4] 99-105 (2003).

73. B.X. Huang, K. Wang, J.S. Church, and Y.-S. Li, "Characterization of oxides on niobium by raman and infrared spectroscopy," *Electrochimica Acta,* 44 [15] 2571-7 (1999).

74. R. Parra, M.S. Góes, M.S. Castro, E. Longo, P.R. Bueno, and J.A. Varela, "Reaction Pathway to the Synthesis of Anatase via the Chemical Modification

of Titanium Isopropoxide with Acetic Acid," *Chem. Mater,* 20 [1] 143-50 (2007).

75. S. Rajesh Kumar, C. Suresh, A.K. Vasudevan, N.R. Suja, P. Mukundan, and K.G.K. Warrier, "Phase transformation in sol–gel titania containing silica," *Mater. Lett,* 38 [3] 161-6 (1999).

76. J.M. Jehng and I.E. Wachs, "ChemInform Abstract: Structural Chemistry and Raman Spectra of Niobium Oxides," *ChemInform,* 22 [15] no-no (1991).

77. R.S. Sonawane, S.G. Hegde, and M.K. Dongare, "Preparation of titanium(IV) oxide thin film photocatalyst by sol–gel dip coating," *Mater. Chem. Phys,* 77 [3] 744-50 (2003).

78. K. Yoshimura, T. Miki, S. Iwama, and S. Tanemura, "Characterization of niobium oxide electrochromic thin films prepared by reactive d.c. magnetron sputtering," *Thin Solid Films,* 281–282 [0] 235-8 (1996).

79. D.A.B. de Filho, D.W. Franco, P.P.A. Filho, and O.L. Alves, "Niobia films: surface morphology, surface analysis, photoelectrochemical properties and crystallization process," *J. Mater.Sci.,* 33 [10] 2607-16 (1998).

80. N. Özer, D.-G. Chen, and C.M. Lampert, "Preparation and properties of spin-coated Nb2O5 films by the sol-gel process for electrochromic applications," *Thin Solid Films,* 277 [1–2] 162-8 (1996).

81. H. Zhang and J.F. Banfield, "Kinetics of Crystallization and Crystal Growth of Nanocrystalline Anatase in Nanometer-Sized Amorphous Titania," *Chem. Mater,* 14 [10] 4145-54 (2002).

82. D.J. Kim, S.H. Hahn, S.H. Oh, and E.J. Kim, "Influence of calcination temperature on structural and optical properties of TiO2 thin films prepared by sol–gel dip coating," *Materials Letters,* 57 [2] 355-60 (2002).

83. X. Chen and S.S. Mao, "Titanium Dioxide Nanomaterials: Synthesis, Properties, Modifications, and Applications," *ChemInform,* 38 [41] no-no (2007).

84. A. Orendorz, A. Brodyanski, J. Lösch, L.H. Bai, Z.H. Chen, Y.K. Le, C. Ziegler, and H. Gnaser, "Structural transformations in nanocrystalline anatase TiO2 films upon annealing in air," *Surf. Sci.,* 600 [18] 4347-51 (2006).

85. R.M. Pittman and A.T. Bell, "Raman studies of the structure of niobium oxide/titanium oxide (Nb2O5.TiO2)," *The J. Physical Chem.,* 97 [47] 12178-85 (1993).

86. W.-X. Xu, S. Zhu, X.-C. Fu, and Q. Chen, "The structure of TiOx thin film studied by Raman spectroscopy and XRD," *Appl. Surf. Sci.*, 148 [3–4] 253-62 (1999).

87. L.J. Hardwick, M. Holzapfel, P. Novák, L. Dupont, and E. Baudrin, "Electrochemical lithium insertion into anatase-type TiO2: An in situ Raman microscopy investigation," *Electrochimica Acta*, 52 [17] 5357-67 (2007).

88. G.-R. Gu, Y.-A. Li, Y.-C. Tao, Z. He, J.-J. Li, H. Yin, W.-Q. Li, and Y.-N. Zhao, "Investigation on the structure of TiO2 films sputtered on alloy substrates," *Vacuum*, 71 [4] 487-90 (2003).

89. N. Mahdjoub, N. Allen, P. Kelly, and V. Vishnyakov, "SEM and Raman study of thermally treated TiO2 anatase nanopowders: Influence of calcination on photocatalytic activity," *Journal of Photochemistry and Photobiology A: Chemistry*, 211 [1] 59-64 (2010).

90. T.D. Robert, L.D. Laude, V.M. Geskin, R. Lazzaroni, and R. Gouttebaron, "Micro-Raman spectroscopy study of surface transformations induced by excimer laser irradiation of TiO2," *Thin Solid Films*, 440 [1–2] 268-77 (2003).

91. R. Olivares-Navarrete, J.J. Olaya, C. Ramírez, and S.E. Rodil, "Biocompatibility of Niobium Coatings," *Coatings*, 1 [1] 72-87 (2011).

92. G. Ramírez, S.E. Rodil, S. Muhl, D. Turcio-Ortega, J.J. Olaya, M. Rivera, E. Camps, and L. Escobar-Alarcón, "Amorphous niobium oxide thin films," *J. Non-Cryst. Solids*, 356 [50–51] 2714-21 (2010).

93. G. Ramírez, S.E. Rodil, H. Arzate, S. Muhl, and J.J. Olaya, "Niobium based coatings for dental implants," *Applied Surface Science*, 257 [7] 2555-9 (2011).

94. E. Eisenbarth, D. Velten, M. Müller, R. Thull, and J. Breme, "Nanostructured niobium oxide coatings influence osteoblast adhesion," *J. Biomed. Mater. Res.Part A*, 79A [1] 166-75 (2006).

95. A. Ochsenbein, F. Chai, S. Winter, M. Traisnel, J. Breme, and H.F. Hildebrand, "Osteoblast responses to different oxide coatings produced by the sol–gel process on titanium substrates," *Acta Biomaterialia*, 4 [5] 1506-17 (2008).

96. H. Maeda, T. Kasuga, and M. Nogami, "Apatite formation on titania–vaterite powders in simulated body fluid," *J. the Euro. Cera. Soc.*, 24 [7] 2125-30 (2004).

97. C.-M. Lin and S.-K. Yen, "Biomimetic growth of apatite on electrolytic TiO2 coatings in simulated body fluid," *Mater Sci and Eng: C*, 26 [1] 54-64 (2006).